Highly dispersed Sn-beta Zeolites as Active Catalysts for Baeyer-Villiger Oxidation: The Role of Mobile, *In Situ* Sn(II)O Species in Solid-State Stannation

Elise Peeters,[a] Guillaume Pomalaza,[a] Ibrahim Khalil,[a] Arnaud Detaille,[b] Damien P. Debecker,[b] Alexios P. Douvalis,[c,d] Michiel Dusselier,[a] and Bert F. Sels*,[a]*

[a] Centre for Sustainable Catalysis and Engineering (CSCE), Leuven Chem&Tech, KU Leuven, Celestijnenlaan 200F, 3001 Heverlee, Belgium

[b] Institute of Condensed Matter and Nanosciences (IMCN), Université catholique de Louvain (UCLouvain), Place Louis Pasteur 1, Box L4.01.09, 1348 Louvain-La-Neuve, Belgium

[c] Mössbauer Spectroscopy & Physics of Materials Laboratory, Department of Physics, University of Ioannina, 45110 Ioannina, Greece

[d] Institute of Materials Science and Computing, University Research Center of Ioannina (URCI), 45110 Ioannina, Greece

Keywords heterogeneous catalysis, Sn-beta zeolite, solid-state incorporation, Lewis acid catalysis, Baeyer-Villiger oxidation, Sn dispersion, inert heating atmosphere, pre-pyrolysis.

ABSTRACT

Solid-state incorporation of Sn into beta (β) zeolites is a fast and efficient method to obtain Lewis acidic Snβ catalysts with high activity. The present work emphasizes the fundamental role of the heat treatment atmosphere on the solid-state incorporation of active Sn in zeolites. Via an array of characterization tools including N_2-physisorption, X-ray diffraction, diffuse reflectance UV-vis,

Fourier transform infrared spectroscopy, X-ray spectroscopy, and ^{119}Sn Mössbauer spectroscopy, it is shown that pre-heating under inert atmosphere (pre-pyrolysis) prior to air-calcination affords Sn-beta catalysts with the highest Sn dispersion and significantly less extra-framework SnO_2 compared to classic calcination. *In situ* characterization during pre-pyrolysis by temperature-programed decomposition-mass spectrometry, thermogravimetric analysis and ^{119}Sn Mössbauer spectroscopy reveals the *in situ* generation of Sn(II)O species that are more mobile than Sn(IV)O_2 species generated during calcination. This mobility property essentially enables the high Sn dispersion in Snβ. Based on this knowledge, active sites per catalyst weight are maximized while retaining high turn-over frequencies for the Baeyer-Villiger oxidation reaction (300 h^{-1} at 80 °C). For Lewis acid densities above 200 $\mu mol \cdot g^{-1}$, the catalytic activity unexpectedly leveled off to 93 $mM \cdot h^{-1}$, even under kinetic control. We tentatively ascribe the activity plateau to the incorporation of Sn in less favorable T-sites at high Sn-loadings.

1. INTRODUCTION

Lewis acidic zeolites, created by incorporation of isolated framework metal centers in a silicate matrix, have gained a lot of attention because of their ability to coordinate hydroxyl and carbonyl groups.[1,2] This affinity toward specific oxygen functionalities renders them pivotal in future biorefinery applications where often oxygenated substrates are converted into valuable chemicals and fuels.[3,4]

Lewis acidic Sn in beta zeolites (BEA framework) in particular, is highly active and selective in a variety of biomass conversion reactions, including (i) sugar isomerization and epimerization of mono- and disaccharides,[5–14] (ii) conversion of sugar(-derived) molecules into lactic acid,[15–17] (iii) aldol reactions,[18,19] (iv) Meerwein-Ponndorf-Verley (MPV) reduction of aldehydes and ketones,[20–23] and (v) H_2O_2-mediated Baeyer-Villiger oxidation (BVO) of ketones.[24–27]

The outstanding performance of Snβ zeolites originates from the tetrahedral incorporation of Sn metal ions in the zeolitic framework vacancies, thereby creating strong Lewis acid sites.[2,28] Snβ zeolites are typically synthesized by a bottom-up hydrothermal (HT) procedure, wherein a hydrated tin precursor (e.g., $SnCl_4 \cdot 5H_2O$ or $SnCl_2 \cdot 2H_2O$) is introduced into the synthesis gel. Next, hydrofluoric acid is added as a mineralizing agent and crystals are formed by treating this mixture under hydrothermal conditions.[24,29] Although HT syntheses produce materials with favorable properties, such as hydrothermal stability and hydrophobicity, several drawbacks prevent its large-

scale implementation. Namely, using hydrofluoric acid lengthens the synthesis time up to 20 days. It also yields large crystals (1-10 μm) that can be detrimental for catalytic performance in diffusion-limited reactions. Moreover, only low amounts of active Sn are typically incorporated (≤2 wt %) resulting in low catalytic productivities when expressed per gram of zeolite.[30] To address these issues, modified HT method have been reported, such as seed-assisted synthesis[31] and steam-assisted dry-gel conversion[32].

Another strategy is to insert Sn atoms into the framework vacancies of dealuminated zeolites in a post-crystallization process. Compared to the bottom-up HT procedures, top-down post-zeolite synthesis methods are faster and easier, produce smaller crystallite sizes, and grant access to higher metal loadings (up to 10 wt %).[30] Post-synthesis (PS) methods typically involve dealumination of (commercial) zeolites via acidic leaching to produce silanol nests, which can act as anchor points for Sn atoms. Such Sn atoms can be introduced via different means including (i) vapor-solid (ii) liquid-solid, and (iii) solid-solid methodologies.[33]

Tin introduction by chemical vapor deposition with anhydrous $SnCl_4$ on dealuminated β zeolites led to Sn loadings up to 6 wt %.[34,35] However, a significant amount of inactive extra-framework tin oxides (SnO_x) is formed during this process. In the liquid-solid method, Snβ zeolites are synthesized via grafting under reflux conditions in dry isopropanol or dichloromethane using hydrated $SnCl_4 \cdot 5H_2O$ and anhydrous $SnCl_4$ as precursor, respectively.[36,37] Grafting with $SnCl_4 \cdot 5H_2O$ in dry isopropanol produced highly active Snβ zeolites on Sn atom basis, but SnO_x appear at Sn loadings higher than 2 wt %.[36] Using dichloromethane as a solvent, up to 6 wt % of Sn can be incorporated in the framework.[37]

In the solid-solid method, dealuminated β zeolites are mechanically ground with tin salts, such as Sn(II) acetate, followed by calcination in air, yielding Sn loadings up to 10 wt %.[38,39] Such solid-state incorporation (SSI) methods are highly convenient as they combine short synthesis times and high final Sn loadings with solvent-free conditions. Consequently, the SSI method is now widely adopted. Despite its popularity, no fundamentals on the Sn incorporation mechanism have been reported. Recently, Hammond et al. made a highly active Snβ catalyst by adding a high-temperature pre-treatment step under nitrogen (N_2) prior to calcination in air.[39] Likewise, Wang et al. applied an intermediate argon (Ar) atmosphere, thereby enhancing the catalytic activity in the MPV reaction.[40] However, to the best of our knowledge, the influence of such a pre-pyrolysis step on the Sn incorporation mechanism, and hence on the catalytic performance, has not been reported.

Therefore, in this paper, we present our study on the fundamental role of inert heat treatment during SSI of Sn on the active site's structure and the catalytic activity of the resulting Snβ catalysts. To do so, we not only investigated the characteristics of the Snβ catalysts after synthesis [by Fourier transform infrared (FTIR), powder X-ray diffraction (PXRD), X-ray photoelectron spectroscopy (XPS), diffuse reflectance UV-vis (DRUV-vis) spectroscopy and ^{119}Sn Mössbauer spectroscopy] but, more importantly, we investigated the Sn species during SSI [by *in situ* ^{119}Sn Mössbauer, temperature-programed decomposition-mass spectrometry (TPDE-MS) and thermogravimetric analysis (TGA)]. Next, their catalytic activity was evaluated in the H_2O_2-mediated BVO of cyclohexanone to ε-caprolactone. Interestingly, our results demonstrate the pivotal role of the Sn-oxidation state during high-temperature SSI in controlling the active site density and hence the catalytic activity per weight Snβ material.

RESULTS AND DISCUSSION

1. Catalytic Performance of Snβ Catalysts in BVO of Cyclohexanone

Several Snβ catalysts were made via SSI with Sn(II) acetate as Sn precursor, varying in both Sn content (1 – 10 wt % Sn) and heat treatment atmosphere. The exact Sn content [in wt %, as determined by inductively coupled plasma-atomic emission spectrometer (ICP-AES)] is listed in Table S1. Two different atmospheres were applied (see Figure S1): (1) a standard calcination (in air at 550 °C for 6h; abbreviated as 'air') and (2) a two-step protocol starting with an inert heat treatment (in N_2 at 550 °C for 3h), followed by calcination (in air at 550 °C for 3h; abbreviated as 'N_2/air'). Samples are denoted as 'XSnβ-Y', wherein X and Y refer to the Sn content (in wt %) and the type of applied heat treatment, respectively.

The Baeyer-Villiger oxidation (BVO) reaction of cyclohexanone (CHO) to ε-caprolactone (CL) was selected as a model catalytic reaction. In this reaction the Lewis acidic Sn activates the carbonyl function of CHO, forming CL through a Criegee intermediate with H_2O_2.[41] To study the effect of the heat treatment atmosphere on the catalytic activity, the as-synthesized Snβ catalysts were monitored by their initial formation rate ($r_{0,CL}$; in $mM_{CL} \cdot L^{-1} \cdot h^{-1}$) as a function of their Sn content (Figure 1). Each $r_{0,CL}$ was determined from the initial linear part of the kinetic plot (see examples in Figure S2). Kinetics were obtained in the kinetic regime. To exclude diffusion limitations, the initial formation rate ($r_{0,CL}$) of the most active catalyst (i.e. 10Snβ-N_2/air) was determined at increasing catalyst mass (expressed as mol % Sn relative to the initial ketone

substrate) while keeping all other reaction parameters constant (see Figure S3). According to Madon-Boudart,[42] interphase mass transfer limitations (i.e. film diffusion limitations) are excluded if doubling of the mass of the catalyst leads to doubling of the reaction rate. Figure S3 shows such a linear relationship between catalyst concentration and initial formation rate, up to a Sn concentration of 0.5 mol %. At higher concentrations, the $r_{0,CL}$ starts to deviate from linearity indicating film diffusion limitations. To avoid film diffusion limitations, we opted for concentrations below 0.5 mol % Sn for all Snβ catalysts tested. In our situation all reactions were therefore performed with 10 mg of catalyst, corresponding to a ketone/Sn molar ratio of 217 (0.46 mol.% Sn) and 2600 (0.04 mol% Sn) for 10- and 1Snβ-N_2/air, respectively. Note that this test cannot exclude pore diffusion limitations, but the assumption that reactions with Sn concentrations below 0.5 mol % occur in the kinetic regime will be confirmed further.

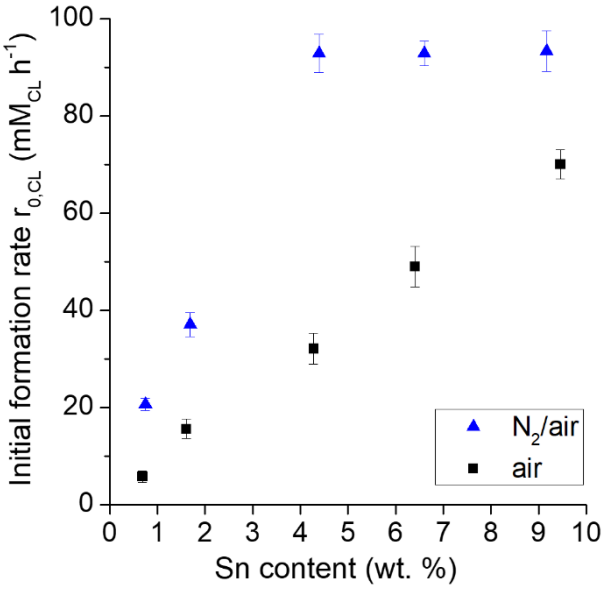

Figure 1. Catalytic activity of Snβ catalysts in BVO reaction in relation to Sn content and heating atmosphere applied during SSI (air: black squares, N_2/air: blue triangles). Reaction conditions BVO: Snβ (10 mg), CHO (330 mM in dioxane), H_2O_2 (50 wt % in dioxane), ratio H_2O_2/ketone = 1.5, 80 °C and 700 rpm. All reactions were performed in triplicate and error bars represent the standard deviation.

As shown in Figure 1, the initial formation rate increased linearly with higher Sn content for Snβ-air catalysts. The Snβ-N_2/air catalysts also followed a positive linear trend at low metal

content, albeit with a steeper slope. At loadings higher than 4 wt % Sn, an activity plateau at ca. 93 $mM \cdot h^{-1}$ was reached for the Snβ-N_2/air catalysts. This plateauing effect will be explained in more detail in part 4. When comparing the two methods at identical Sn content, the Snβ-N_2/air catalysts always surpassed the Snβ-air catalysts in terms of $r_{0,CL}$. For instance, at a Sn content of approximately 4.2 wt %, the $r_{0,CL}$ for N_2/air is almost 3 times that of the air catalyst. These results were independent of the gas flow regime (static or in flow) applied during heat treatment (see details in Materials and Methods). The results clearly show that a pre-pyrolysis step during solid-state synthesis markedly improves the catalytic activity of the Snβ zeolite in agreement with recent literature.[39,40]

In the next section, we first investigate the improved physicochemical properties of the Snβ catalysts treated by a pre-pyrolysis step. Thereafter, we scrutinize the influence of inert heat treatment on the Sn incorporation mechanism.

2. Solid-State Characterization of Snβ Catalysts after Synthesis

2.1. Framework Sn and/or Extra-Framework SnO_2

To explain the superior activity of catalysts prepared via pre-pyrolysis, we characterized several Snβ catalysts using a variety of solid-state characterization tools. First, we evaluated the effect of the heating step on the formation of framework and extra-framework Sn. Elemental composition (in wt %) was determined by ICP-AES, and porosity data (in $cm^3\ g^{-1}$) were obtained by N_2-physisorption analysis, as listed in Table S1 for the parent, dealuminated and Sn-incorporated β zeolites. The N_2-physisorption data showed micropore volumes between 0.19 – 0.24 $cm^3 \cdot g^{-1}$ and total pore volumes of 0.31 – 0.34 $cm^3 \cdot g^{-1}$ for all samples. The similar pore volume suggests that no pore volume is blocked due to the presence of extra-framework SnO_2. However, this does not exclude pore blockage since the BEA topology displays interconnected 3D channels which allows to circumvent local obstructions in the pores.

Powder X-ray diffraction (PXRD) data, shown in Figure 2, indicate the parent β zeolite signature diffraction pattern in all samples. Therefore, the β structure remains intact throughout dealumination and Sn incorporation. If present, extra-framework SnO_2 particles can be detected by PXRD provided that these are crystalline, large enough, and present above the detection limit of 0.5 wt % of crystalline SnO_2.[43] Signature Bragg reflections arising from pure crystalline SnO_2 (reference) gradually appeared for Snβ-air samples at 5 wt % of Sn and intensified at higher Sn content. The crystallite sizes of SnO_2 of the air-treated samples can be estimated from XRD line

broadening by Debye-Scherrer equation (see Materials and Methods).[44,45] Crystallite sizes of 7.7, 7.0 and 5.4 nm were obtained for 10-, 7-, and 5Snβ-air, respectively. For comparison, when SnO_2 was used as precursor (Figure 2, [SnO_2 + deAlβ]-air), the crystallite size of SnO_2 was 18.8 nm. Notably, such SnO_2 reflections were absent for Snβ-N_2/air samples even at a loading of 10 wt % of Sn. However, the absence of SnO_2 reflections does not mean that extra-framework SnO_2 species are absent as particles smaller than 5 nm are below the detection limit.

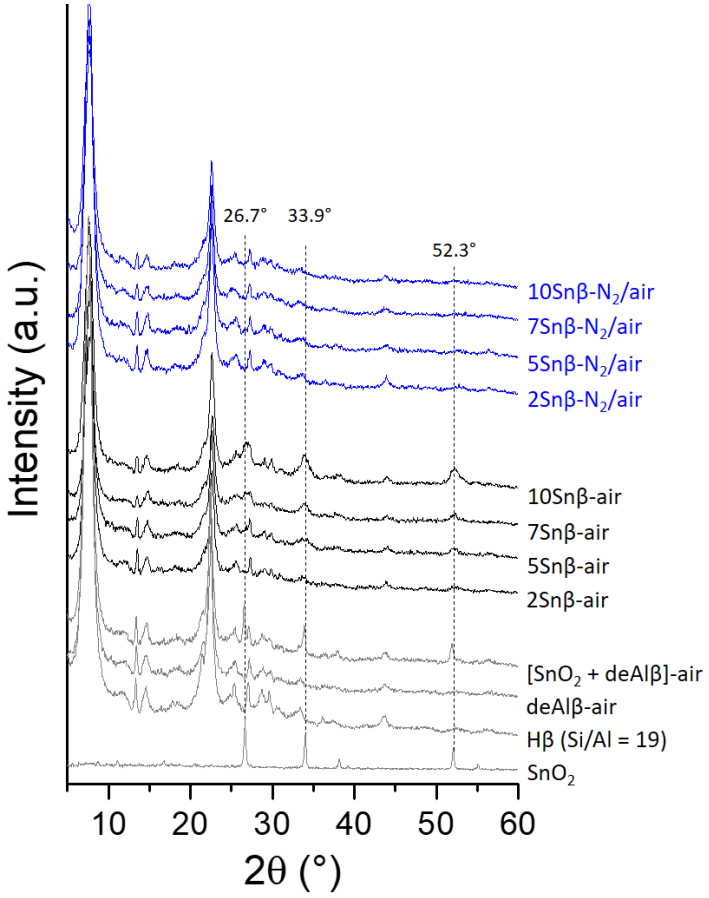

Figure 2. PXRD patterns of pure SnO_2, parent Hβ (Si/Al = 19), calcined dealuminated β (deAlβ-air), calcined deAlβ with SnO_2 (2 wt % Sn), and the Snβ samples with varying Sn content and heat treatment (air: black, blue: N_2/air). The calcined deAlβ with SnO_2 was synthesized according to the standard calcination but instead of Sn(II) acetate, SnO_2 was used as a precursor. SnO_2 signature Bragg reflections are indicated by dashed lines.

The presence of extra-framework SnO_2 was also investigated by DRUV-vis spectroscopy, which exploits the electronic properties of Sn via the electronic transfer from the surrounding O-atoms towards the unoccupied orbital of Sn (ligand to metal charge transfer). After sample conditioning

in air at 550 °C, DRUV-vis spectra of dried samples showed resonances at 210 and 265 nm (Figure 3A). The resonance at 210 nm is typically assigned to isolated tetrahedrally coordinated framework Sn generated by isomorphous substitution, while the resonance at 265 nm is attributed to octahedrally coordinated extra-framework SnO_2 particles.[36,46] At increasing Sn content, the intensity of the framework Sn band (210 nm) increased for all samples, but this is more pronounced for Snβ-N_2/air samples, meaning that more Sn is incorporated in the framework. Meanwhile, less Sn is present as large extra-framework SnO_2 particles as confirmed by the low intensity at 265 nm compared to the air-calcined catalysts. This trend was semi-quantified by calculating the framework/extra-framework Sn-ratio from the peak areas at 210 and 265 nm in Table S2. An example of a deconvoluted DRUV-vis spectrum is shown in Figure S4. The better Sn incorporation into the β framework for the N_2/air-treatment was reflected by its three- to four-fold higher framework/extra-framework ratio compared to the air-calcined samples. While the ratio is quasi-constant for all Snβ-air catalysts at the different Sn contents, the framework/extra-framework ratio decreases from 2.2 to 1.6 for Snβ-N_2/air samples with a Sn loading beyond 5 wt %. This is most likely explained by the formation of more spectator sites in the form of Sn oxide oligomers and/or extra-framework SnO_2 at high Sn loadings.[39]

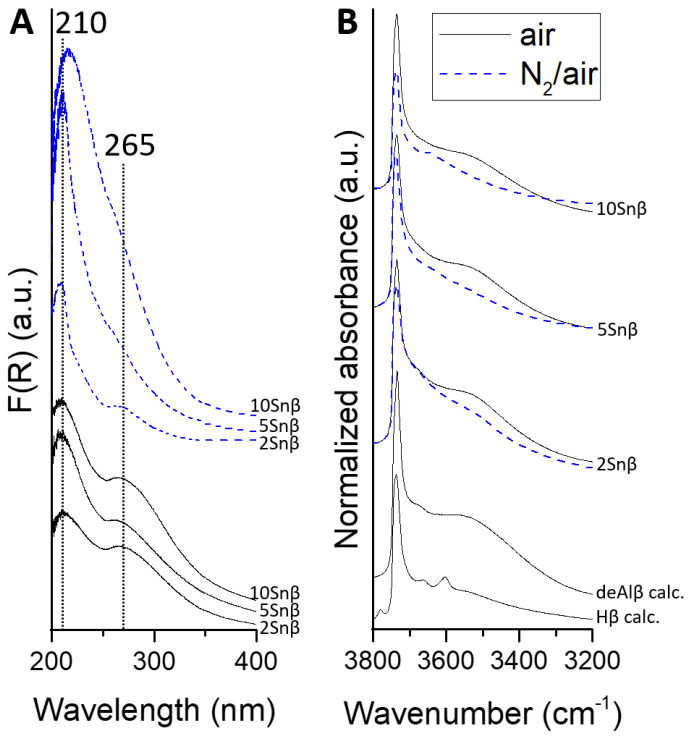

Figure 3. (A) DRUV-vis and **(B)** FTIR spectra for selected (Sn)β catalysts treated in different heating atmospheres (air: black full line, N_2/air: blue dotted line) with the Sn content (X) denoted as XSnβ. For DRUV-vis, samples were dried at 550 °C under flowing air prior to measurement. For FTIR, samples were dried at 400 °C for 1 h under vacuum prior to measurement at 150 °C. The spectra show the silanol region normalized by the total T-O-T overtone area (2100 – 1750 cm^{-1}).[22,47] Note that Hβ (parent β zeolite [Si/Al = 19]) and deAlβ (dealuminated β-zeolite) are also calcined in air at 550 °C.

Further indirect evidence of greater Sn framework incorporation for Snβ-N_2/air catalysts was gathered with the surface XPS technique. XPS spectra of our Snβ samples (Figure S5B) display signals of Sn $3d_{3/2}$ and $3d_{5/2}$ with binding energies at 495.8 and 487.5 eV, respectively, which is indicative of Sn(IV).[43] In Figure S5A the Sn/Si ratio at the surface (XPS) and bulk (ICP) is plotted. The higher surface Sn/Si ratio of 7Snβ-air compared to 7Snβ-N_2/air shows that less Sn species are infiltrated into the zeolite. This could suggest that the Sn species formed during air-calcination are too large to enter the beta zeolite crystal or they are less mobile to disperse (*vide infra*).

Formation of framework Sn by SSI of Sn was also monitored by calculating the amount of residual silanols via FTIR spectroscopy. Figure 3B shows the FTIR spectrum of the parent H-β

zeolite with specific stretches at 3781, 3740, 3665 and 3609 cm^{-1}, corresponding to hydroxyl groups bonded to extra-framework Al [such as AlO(OH)], terminal silanol groups, low acidic perturbed Al-OH groups, and structural Si(OH)Al groups, respectively.[48–50] After dealumination, the Al-related bands (3781, 3665 and 3610 cm^{-1}) disappear and a broad band appears between 3600 – 3500 cm^{-1}, which can be assigned to hydrogen-bonded Si-OHs at defect framework sites—so-called silanol nests.[48–50] The normalized silanol population (3800 – 3300 cm^{-1}) on Snβ samples with the same Sn content but different heat treatment are compared in Figure 3B. Samples were activated at 400 °C under vacuum to remove water. For all Sn loadings, the Snβ-N_2/air catalysts have lower residual silanol content compared to the air-treated catalysts. No absolute quantitative analysis is possible given that the molar absorption coefficient of silanols strongly depends on H-bonding interactions.[51] Still, semi-quantitative data can be derived by carefully calculating the relative decrease in normalized silanol area (3800-3200 cm^{-1}) compared to the air-calcined dealuminated β.[52] Note that a possible influence of the heat treatment on the silanol content was eliminated by using a calcined dealuminated β. As seen from Table S2, all Snβ samples show a relative decrease in silanol area, which is approximately two-fold higher for Snβ-N_2/Air *versus* Snβ-air samples at similar Sn content. This proves that Sn is better incorporated into the framework silanol nests for Snβ-N_2/air samples, thereby supporting the PXRD, DRUV-vis and XPS data.

Finally, we turned to ^{119}Sn Mössbauer spectroscopy to investigate the Sn-oxidation state and its interaction with the zeolite matrix. (Table 1, Figure S6). As illustrated in Table 1, only Sn(IV) was detected on Snβ-air catalysts, whereas some residual Sn(II) (up to 6%) remained on Snβ-N_2/air samples. Note that even prolonged heating under air (6 h) was unable to oxidize the residual Sn(II) into Sn(IV) (Table 1, line 6). This low amount of residual Sn(II) can, however, not be invoked to explain the increased catalytic activity of the N_2/air samples. In the BVO reaction, the Lewis acid strength is of importance since the carbonyl group of the substrate is activated by Lewis acidic Sn center. As the Lewis acid strength of Sn(II) is lower than Sn(IV),[53] we can deduce that Sn(II) is not as active as Sn(IV) in the BVO. Apart from the oxidation states, we found a striking difference in the quadrupole splitting (QS) and isomer shift (IS) values of the Sn(IV) sites. For the pre-pyrolysis samples, the higher QS values (0.7 *vs.* 0.5 $mm \cdot s^{-1}$ for N_2/air and air, respectively) and the more negative IS values IS (-0.06 to -0.10 for N_2/air *vs.* 0.01 to 0.03 for air), suggest a more distorted first neighbor environment and a different interaction of the Sn(IV) ions with the zeolite matrix relative to the air-treated samples.[54–56] This is further confirmed by the reduced absorption

depth (effect) difference between the 77 K and RT recorded spectra of each sample (expressed as Δeffect/effect at 77 K) (Table S3, Figure S6 and S7). The absorption depth (or effect) is the highest absorption point value of the spectrum taken from the 100% non-resonant baseline. To eliminate the mass of each sample, the difference in effect (between 77 K and RT) is divided by the effect value at 77 K. The reduced effect difference gives a rough estimate of the firmness of binding of the incorporated Sn(IV) ions in the zeolite matrix.[57] This difference is higher for the N_2/air-treated samples (74-77%) than the air-treated samples (46-58%). This indicates different bonding interactions of the Sn(IV) ions' sub-lattice to the zeolite matrix in the case of the N_2/air-treated samples, which could result from the higher number of incorporated Sn(IV) ions or/and the presence of the additional Sn(II) ions. Hence, IS, QS and Δeffect/effect at 77 K point to an - on average - higher incorporation of Sn in the framework of an inert treated catalyst.

Table 1. **Best-fit ^{119}Sn Mössbauer Parameters for the Selected Snβ Samples**

entry	sample	AA [Sn(IV)/Sn(II)] (%/%)	IS[a] ($mm \cdot s^{-1}$)	QS[a] ($mm \cdot s^{-1}$)
1.	2Snβ-air	100/0	0.02	0.52
2.	5Snβ-air	100/0	0.01	0.50
3.	10Snβ-air	100/0	0.03	0.53
4.	2Snβ-N_2/air	94/6	-0.10 (3.16)	0.65 (1.84)
5.	10Snβ-N_2/air (3 h air)	95/5	-0.06 (3.37)	0.75 (1.77)
6.	10Snβ-N_2/air (6 h air)	96/4	-0.06 (3.19)	0.72 (1.53)

[a] data derived from spectra at 77 K. Values of the remaining Sn(II) in parenthesis. Abbreviations: AA, absorption area; IS, isomer shift; QS, quadrupole splitting

2.2 Lewis Acid Density and Sn Dispersion

As observed with the results of PXRD, DRUV-vis, XPS, FTIR and ^{119}Sn Mössbauer spectroscopy, the inert heat treatment favors the incorporation of Sn within the zeolite framework

rather than forming extra-framework SnO_2 particles. Therefore, the improved catalytic activity of Snβ-N_2/air catalysts (Figure 1) may be related to the increased Lewis acid (LA) density as tetrahedrally coordinated Sn(IV) sites exhibit strong Lewis acidity.

The amount of LA sites was probed via FTIR spectroscopy of adsorbed pyridine. As an example, the FTIR spectra of pyridine adsorbed on 5Snβ-air is provided in Figure S8. The resonance bands at 1611, 1491, and 1451 cm^{-1} were assigned to pyridine adsorbed on LA sites. Features at 1597, 1576, and 1445 cm^{-1} correspond to H-bonded pyridine with the OH groups.[34,58–60] The absence of a resonance band at 1545 cm^{-1} indicated that Brønsted acid sites are absent in Snβ zeolite samples, which is in line with the low Al content ($SnO_2/Al_2O_3 > 2000$, as a result of the deep dealumination). The LA density was calculated from the spectra (see details in Materials and Methods) by using a molar extinction coefficient of 1.42, as determined by Gounder et al. for LA Sn sites.[59]

Figure 4A plots the LA density in $\mu mol_{LA} \cdot g_{catalyst}^{-1}$ against Sn content in wt %. Whereas the Snβ-air catalysts follow an almost linear trend, the Snβ-N_2/air catalysts significantly deviate from linearity at Sn loadings above 5 wt %. This is likely due to the formation of more spectator sites in the form of Sn oligomers resembling the extra-framework SnO_2 observed at higher Sn loadings.[39] In addition, the LA density of the Snβ-N_2/air catalysts is almost tripled relative to the Snβ-air catalysts at identical Sn content. Hence, more LA Sn sites are formed when the SSI procedure starts in an inert atmosphere.

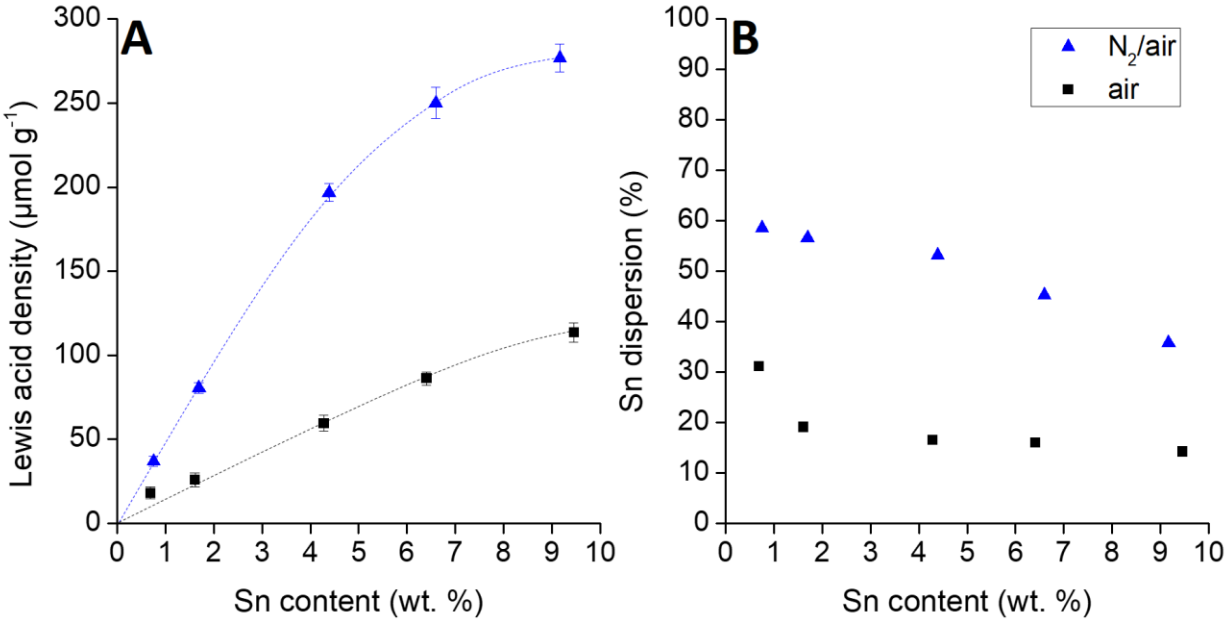

Figure 4. Snβ catalyst characteristics in relation to heating atmospheres applied during SSI (air: black squares, N_2/air: blue triangles). (A) Lewis acid density and (B) Sn dispersion as a function of Sn content. Lewis acid density was measured by pyridine-FTIR spectroscopy at 150 °C and calculated with an integrated molar extinction coefficient (ε) of 1.42 cm·μmol^{-1}.[59] The total Sn content was quantified by ICP-AES. The Sn dispersion is the total amount of active Sn sites, as determined by pyridine-FTIR (assuming 1 active Sn site per adsorbed molecule of pyridine) divided by the total amount of Sn atoms. Pyridine-FTIR of the catalysts were obtained in duplicate. Error bar represents the standard deviation.

The increase in active Sn sites for the inert-heated samples can also be expressed in terms of Sn dispersion (in %). Figure 4B depicts the Sn dispersion against Sn content by assuming one adsorbed pyridine molecule per active Sn site.[59] A maximal dispersion of almost 60% was reached for Snβ-N_2/air catalysts at 1 wt % of Sn, while only 31% was detected for the standard calcination method. This maximal dispersion is in line with literature values reported for SSI-Snβ catalysts (1.5 wt % Sn) made via N_2/air protocol (59%)[61] and a HT-Snβ catalyst (65% for Snβ having low Sn content (<1 wt %); recalculated values using 1.42 as molar extinction coefficient).[53]

Next, a positive correlation was found between the relative decrease in normalized silanol area and the LA density (Figure 5). This confirms that LA sites are formed by the incorporation of Sn into the framework silanol nest.

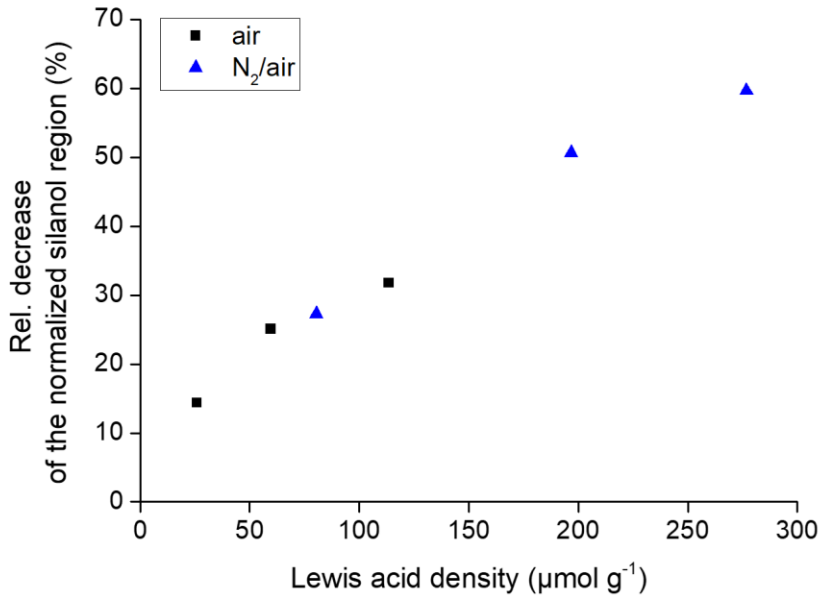

Figure 5. Linear decrease ($R^2 > 0.98$) in the normalized silanol area as a function of the Lewis acid density for Snβ-(N_2/)air zeolites (air: black squares, N_2/air: blue triangles). The linear decrease of the silanol area is calculated relatively to the silanol area of a calcined dealuminated beta and normalized by the total T-O-T overtone area (2100 – 1750 cm^{-1}).[22,47]

By plotting $r_{0,CL}$ against LA density (Figure 6), we attempted to find a common basis governing catalytic activity, irrespective of the heat treatment used. From this, an initial positive linear relationship was seen between $r_{0,CL}$ and LA density, correlating the data points of both calcination methods at LA densities up to approximately 200 $\mu mol \cdot g^{-1}$. At higher LA density (200 $\mu mol_{LA} \cdot g^{-1}$ and up), the initial formation rate plateaued at 93 $mM_{CL} \cdot h^{-1}$. This suggests that – independently of the heating atmosphere used – the BVO activity is linearly correlated to the total amount of LA sites up to a maximum of 93 $mM_{CL} \cdot h^{-1}$ at 200 $\mu mol \cdot g^{-1}$. A similar leveling off in activity has been observed with BVO of 2-adamantanone[34] (Figure S9), and for another reaction type, namely the glucose to methyl lactate conversion.[17] However, no explanation was given for this effect.

A possible explanation for this effect could be that only the amount of closed framework Sn sites increases while no extra open framework Sn sites are formed at LA density above 200 $\mu mol \cdot g^{-1}$. Boronat et al. (2005) indeed reported that in HT Snβ only open (and not closed) framework Sn sites are active in BVO. Closed framework Sn sites are tetrahedrally coordinated to framework oxygen, whereas open Sn sites display only threefold framework coordination and one hydroxyl group.[62] To this effect, we also performed CD_3CN-FTIR spectroscopy (see Figure S10) since pyridine as a probe molecule is unable to discriminate open and closed Sn sites.[59,62] The plot of the catalytic activity against open Sn sites (Figure S11A) revealed similar leveling off at high LA density. Moreover, in contrast to Boronat et al. (2005),[62] the closed Sn sites (Figure S11B) of our PS Snβ zeolites display the same trend. From these data, it is therefore not possible to deduce if only open Sn sites are active in the BVO reaction.

Furthermore, as previously reported by our group, it should be noted that not only framework Sn sites, but also small SnO_x species in PS Snβ are active for BVO, albeit to a lesser extent (expressed as activity per Sn).[36] Recently, this was confirmed by Dai et al.,[63] who showed that small SnO_2 clusters (with a size up to 2 nm) confined in PS Snβ zeolites possess a BVO catalytic activity comparable to isolated framework Sn sites.[63] Since such species show Lewis acidic characteristics similar to isolated framework Sn sites, they will also contribute to the total LA

density as calculated by Py-FTIR. Therefore, to not exclude potential active Sn sites for the BVO reaction, we decided to proceed with the total LA density.

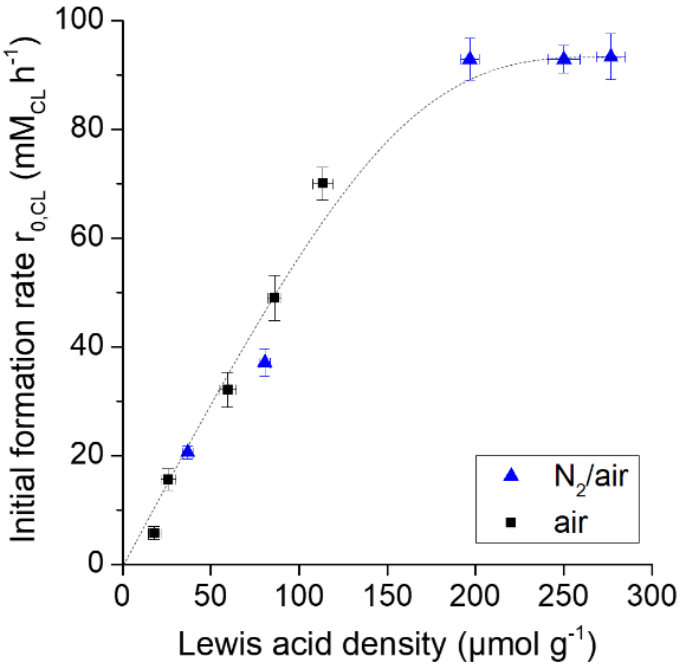

Figure 6. Initial formation rate in relation to Lewis acid density and heating atmosphere applied during SSI (air: black squares, N_2/air: blue triangles). Reaction conditions BVO: Snβ (10 mg), ketone (330 mM in dioxane), H_2O_2 (50 wt % in dioxane), H_2O_2/ketone ratio of 1.5, 80 °C and 700 rpm. Lewis acid density was measured by pyridine-FTIR spectroscopy at 150 °C, and calculated with an integrated molar extinction coefficient (ε) of 1.42 cm.µmol^{-1}.[59] Total Sn content was quantified by ICP-AES. Pyridine-FTIR of the catalysts and the BVO reaction were performed in duplicate and triplicate, respectively. Error bars represent the standard deviations.

In Figure S12, the turnover frequency (TOF) of the different catalysts is plotted against its LA density. The TOF is calculated by dividing the intrinsic activity, which is determined based on the amount of CL formed after 10 minutes of reaction, by the active Sn site density (measured via Py-FTIR). Up to a LA density of 200 µmol·g^{-1}, the observed TOF is quasi constant (around 300 h^{-1}) for both heating atmospheres, suggesting that identical species are the dominant active sites. At higher LA densities a sharp decrease in TOF is apparent. The activity plateau and decrease in TOF with increasing Sn content will be further discussed in part 4.

As summarized, the observed disparity in the activity of Snβ catalysts made via different heat treatments can be explained on the basis of LA density: (i) the catalytic activity is proportional to

the overall LA density up to a certain maximum (Figure 6), and (ii) the pre-pyrolysis step increases the LA density by promoting Sn dispersion, e.g., 2Snβ-N_2/air outperforms 5Snβ-air (Figure 4 and 6). The higher LA density of the samples with the pre-pyrolysis step resulted from a better incorporation of Sn in the zeolite framework. Via a toolset of characterization techniques we observed that the direct oxidation in air without the intermediate N_2-step increased the amount of large extra-framework SnO_x clusters which is visualized by (i) SnO_2 reflections that arise in the PXRD pattern at Sn loading >5 wt % (PXRD) (ii) the extra-framework Sn band at 265 nm (DRUV-vis), (iii) less decreased silanol area after Sn incorporation (FTIR), (iv) a higher amount of Sn on the catalyst surface compared to the bulk Sn (XPS/ICP) and (v) a lower QS, a higher IS, and a smaller temperature-dependent absorption depth difference, leading to a less distorted and firmer-bonded first neighbor environment (^{119}Sn Mössbauer spectroscopy).

Based on the catalytic and characterization data, we hypothesize that the accrued Sn dispersion and catalytic activity obtained by using a pre-pyrolysis step results from the persistence of Sn(II) species during a crucial step of the synthesis process. We argue that the Sn(II) species, present in the Sn(II) acetate precursor, are rapidly oxidized to Sn(IV) in heated air, whereas the Sn(II) retains its oxidation state during the SSI under inert atmosphere.

3. Solid-State Characterization of Snβ Catalyst during Synthesis

To corroborate this hypothesis, we investigated the existence of Sn(II) species during inert heat treatment by ^{119}Sn Mössbauer spectroscopy (Figure 7). While Sn is only present in the +4 oxidation state in Snβ samples treated for 3 h at 550 °C in air (Figure 7A), 82% of the Sn in Snβ samples treated for 3 h at 550 °C in N_2 remains in the +2 oxidation state (Figure 7B). These findings confirm our hypothesis. However, they are in contrast to a recent paper by Joshi et al. who suggested that Sn(II) already oxidizes to Sn(IV) during the mixing process prior to heat treatment.[47] This early oxidation might have been triggered by their use of high-energy ball milling as opposed to the low-energy manual grinding used in this study. Furthermore, the authors suggested the oxidation state of Sn based on XPS and K-edge XANES analysis, both of which are unable to unambiguously discriminate between Sn(II) and Sn(IV) when present in low amount.[64]

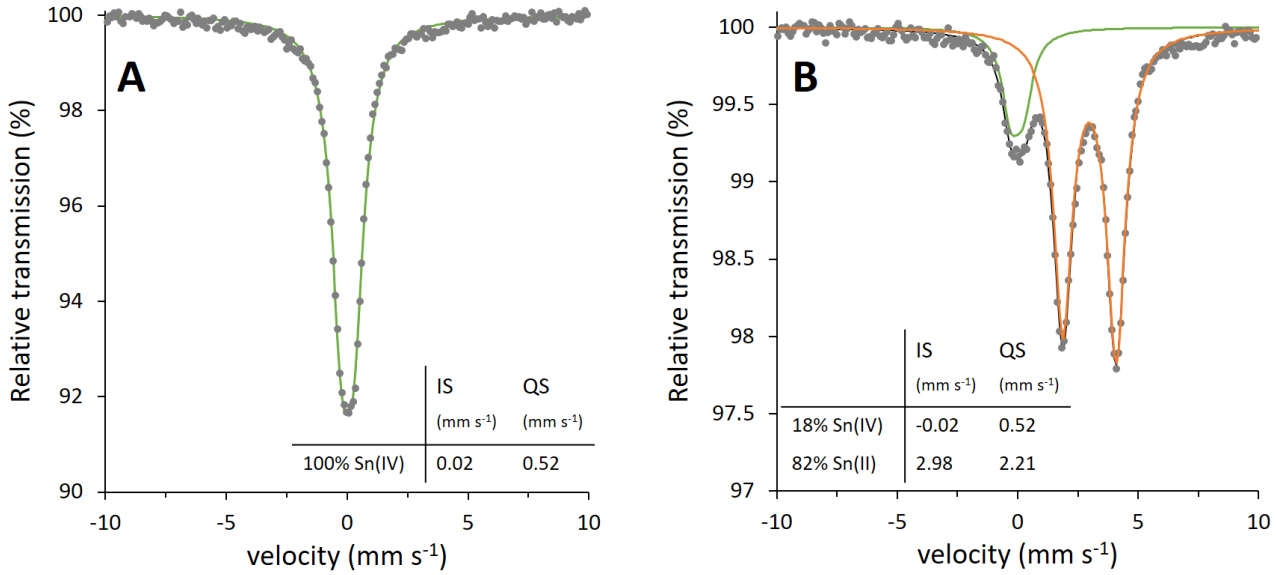

Figure 7. 77 K ^{119}Sn Mössbauer spectra of 2Snβ after **(A)** 3 h at 550 °C in air and **(B)** 3 h at 550 °C in N_2. The points correspond to the experimental data and the colored continuous lines correspond to the components used to fit the spectra [green, Sn(IV); orange, Sn(II)]. Percentages of Sn(IV) and Sn(II) are given in the inset table together with the corresponding quadrupole splitting (QS) and isomer shift (IS).

To get insight into the characteristics of the Sn species that are present during the different heat treatments, we examined the gaseous decomposition products formed during Snβ synthesis using TPDE-MS (Figure S13). TPDE-MS was performed using catalyst pellets made from a mixture of Sn(II) acetate and deAlβ (5 wt % Sn), manually ground for 10 min. From the TPDE-MS data (Figure S13) three clear decomposition-temperature ranges were identified. First, between 275 and 500 °C, acetone (m/z = 58) and CO_2 (m/z = 44) were detected in an inert atmosphere. Note that acetone is relatively absent in the same temperature range in oxidizing conditions. Second, between 275 and 350 °C, acetic acid (m/z = 45), water (m/z = 18) and CO_2 (m/z = 44) were exclusively detected in the oxidizing conditions. Third, between 200 and 275 °C under either atmosphere, acetic acid (m/z = 45) and CO_2 (m/z = 44) were formed while water (m/z = 18) was consumed. The gradual release of water at lower temperature (50 – 250 °C) was attributed to both physi- and chemisorbed water, which is present on the dealuminated β and Sn precursor.[47]

Supported by the observed temperature range of decomposition, we can derive a series of chemical equations describing the thermal decomposition of Sn(II) acetate in the presence of

zeolite during SSI. At T ≤ 275 °C, an hydrolysis reaction occurs in which Sn(II) acetate hydrolyzes to Sn(II)O and acetic acid in the presence of water under both atmospheres (eq 1). Such acetic acid formation was also suggested for anhydrous Zn(II) acetate in the presence of water vapor at 250 °C.[65] However, at temperatures higher than 275 °C, two different pathways become apparent. In oxidizing atmosphere, the produced acetic acid is ostensibly combusted to CO_2 and H_2O between 275 and 350 °C (eq 2). The produced water further promotes hydrolysis of Sn(II) acetate to acetic acid (eq 1). The SnO species are further oxidized to SnO_2 under the air conditions as already proven by the aforementioned ^{119}Sn Mössbauer spectroscopy results (eq 3). In inert conditions in presence of the zeolite, Sn(II) acetate seems to decompose to SnO, acetone and CO_2 between 275 and 500 °C (eq 4). Indeed, Donaldson et al. also reported SnO, acetone and CO_2 and no acetic acid as the thermal decomposition products of pure Sn(II) acetate in inert atmosphere.[66] Finally, reports also mentioned the disproportionation of bulk SnO into metallic Sn and SnO_2 and/or Sn_2O_3 (or $SnO{\cdot}SnO_2$) at 550 °C in inert atmosphere.[67,68] However, we exclude this possibility because no metallic Sn was detected with ^{119}Sn Mössbauer spectroscopy (otherwise clearly visible at an IS of approximately 2.6 $mm{\cdot}s^{-1}$) after 3 h in inert atmosphere at 550 °C (*vide supra*).

At T ≤ 275 °C in both atmospheres

$$Sn^{II}(CH_3COO)_2 + H_2O \rightarrow Sn^{II}O + 2CH_3COOH \quad (1)$$

At 275 ≤ T ≤ 350 °C in oxidizing atmosphere

$$Sn^{II}(CH_3COO)_2 + H_2O \rightarrow Sn^{II}O + 2CH_3COOH \quad (1)$$

$$CH_3COOH + 2O_2 \rightarrow 2CO_2 + 2H_2O \quad (2)$$

$$2Sn^{II}O + O_2 \rightarrow 2Sn^{IV}O_2 \quad (3)$$

At 275 ≤ T ≤ 500 °C in inert atmosphere

$$Sn^{II}(CH_3COO)_2 \rightarrow Sn^{II}O + CH_3COCH_3 + CO_2 \quad (4)$$

By balancing the stoichiometry of eqs 1, 3 and 4, we expect that decomposition of zeolite-associated Sn(II) acetate delivers SnO and SnO_2 in inert and oxidizing atmospheres, respectively. The thermodynamically unstable SnO species are easily transformed to SnO_2 in oxidizing conditions but remain (meta)stable in inert conditions in the zeolite β.

Finally, TGA was applied to detect weight changes indicative of SnO_2 formation during the oxidizing heat treatment step. In a first experiment, commercial bulk SnO increased in weight in O_2-flow starting at 525 °C (results not shown). This agrees well with literature that states that oxidation of pure SnO proceeds via an intermediate Sn_2O_3 (or $SnO{\cdot}SnO_2$) phase at 525 °C before transitioning to a more thermodynamically stable SnO_2 phase at 600 °C.[67] However, because the oxidation onset temperature of metal oxide nanoparticle decrease with their size,[69,70] the oxidation of the small SnO species present in the zeolite is likely expected to take place at lower temperature. In a second experiment, both Snβ catalyst (5 wt % Sn) synthesis methods were mimicked during TGA by grinding Sn(II) acetate with deAlβ and selecting the carrier gas (Figure S14). In O_2, the residual weight at 550 °C remained practically constant for 6 h. Contrarily, the residual weight at 550 °C was significantly lower during the first 3 hours in N_2. This discrepancy is presumably caused by the difference in molar mass between SnO (134.71 $g{\cdot}mol^{-1}$) and SnO_2 (150.71 $g{\cdot}mol^{-1}$) in the sense that the lower residual weight observed under N_2 indicates that SnO was not fully oxidized. Interestingly, this discrepancy in residual weight at 550 °C rapidly disappeared upon switching from an N_2 to an O_2 atmosphere, further supporting our oxidation state hypothesis.

The complementarity among the TPDE-MS, TGA and ^{119}Sn Mössbauer spectroscopy results confirms our oxidation state hypothesis, which links the improved Sn dispersion to *in situ*-generated of Sn(II)O species. From a physical point of view, this might be explained by the volatility (and hence the mobility) of the Sn species, as can be expressed in terms of vapor pressure. For bulk powders, Sn(II)O possesses a higher vapor pressure compared to $Sn(IV)O_2$.[71] At 1000 °C, for instance, the vapor pressure of Sn(II)O lies above 10 mbar, while for $Sn(IV)O_2$ the vapor pressure is only 0.34 mbar.[71,72] Based on this, one might expect Sn(II)O to be more mobile than $Sn(IV)O_2$ at identical temperature, making it more likely for Sn(II)O to disperse through the zeolite than $Sn(IV)O_2$. Instead of bulk $Sn(IV)O_2$ and Sn(II)O, the zeolitic material contains small Sn(II)O and $Sn(IV)O_2$ species. As vapor pressure increases when reducing the $SnO_{(2)}$ particle size,[73,74] the actual vapor pressure of such $SnO_{(2)}$ species in the zeolite will thus be higher.

Once in their mobile state, such *in situ*-generated mobile Sn-oxide species seek to lower their surface free energy. To do so, Sn-oxide species will either (i) sinter into larger particles (cohesion) or (ii) interact with the zeolitic support (adhesion) through the silanol nests, thereby increasing the Sn dispersion.[75,76] The most energetically favored mechanism will be dominant. Recently, it was reported that the adsorption energy (ΔE_{ads}) of PtO_x on the surface of CeO_2, as calculated via DFT,

is always higher for Pt(II)O than Pt(IV)O_2 (in absolute values).[75,77] In line with these findings, it could be hypothesized that interaction with the silanol nests within the zeolitic support is more energetically favorable for Sn(II)O than for Sn(IV)O_2. This might be originating from its (i) lower coordination number, and (ii) smaller molecular size, facilitating the silanol nest insertion. Such dominant adhesion forces can ensure a strong anchoring of atomically dispersed metals onto the zeolite support thereby preventing metal oxide sintering.[78]

Finally, one could argue that Sn(II) acetate itself is by default mobile because of its low melting point (180 °C) and the inert treatment only serves to distribute Sn(II) acetate evenly in the zeolite before its decomposition to Sn(II)O (at approximately 240 °C). To evaluate which factor dominates the Sn-distribution process (melted Sn(II) acetate *vs*. decomposition in Sn(II)O species), we adapted the synthesis protocol with a focus on the melting time. In a first protocol, the duration of the melted, non-decomposed Sn(II) acetate in inert atmosphere was prolonged. To do so, the Sn(II) acetate ground with dealuminated beta was heated to 190 °C under N_2-flow. After 3 h under inert atmosphere at 190 °C, the atmosphere was switched to air and the sample was calcined at 550 °C for 3 h (abbreviated as 5Snβ-melt). In a second protocol, the melting time was reduced by increasing the heating rate from 2 to 10 °C·min^{-1} (abbreviated as 5Snβ-N_2/air-fast).

The DRUV-vis spectrum (Figure S15a) of 5Snβ-melt is similar to air-calcined Snβ (5Snβ-air), showing a high amount of extra-framework SnO_2. Compared to 5Snβ-air, the 5Snβ-melt catalyst gives a slight increase in activity (42 vs. 32 $mM_{CL}\cdot h^{-1}$). However, 5Snβ-N_2/air is still more than twice as active (93 $mM_{CL}\cdot h^{-1}$). In contrast, a reduction in melting time (5Snβ-N_2/air-fast) gives a catalyst with a similar DRUV-vis spectrum (Figure S15b) and catalytic activity (92 $mM_{CL}\cdot h^{-1}$) as the 5Snβ-N_2/air catalyst. Hence, it seems that not melting but decomposition of Sn(II) acetate in inert atmosphere is the dominant factor governing Sn-dispersion.

In summary, the decomposition of Sn(II) acetate to Sn(II)O during inert pre-pyrolysis induces a higher Sn dispersion compared to air calcination because Sn(II)O is more mobile than Sn(IV)O_2, which increases its probability to encounter zeolitic silanol nests. Moreover, the interaction between the silanol nests and Sn(II)O is supposedly stronger, favoring the anchoring of Sn in the framework.

4. Catalytic Activity Plateau at Higher LA Density

Although our reaction conditions were set to exclude interphase mass transfer limitations according to the Madon-Boudart test (see section 1, Figure S3),[42] intraphase mass transfer

limitations (i.e. intracrystalline pore diffusion limitations) might still be present and this may be the most obvious explanation why the catalytic activity levels off at LA densities above 200 $\mu mol \cdot g^{-1}$ (Figure 6).

To investigate pore diffusion, we first applied the well-known Koros-Nowak criterion, which states that the concentration of active material per amount of catalyst is directly proportional to the reaction rate in kinetic regime.[42,79] Assuming that the concentration of active material per amount of catalyst is equal to the total LA density, this criterion is tested in Figure 6. It suggests that the reaction is in kinetic regime up to 200 $\mu mol \cdot g^{-1}$ after which the catalytic activity plateaus due to pore diffusion limitations. However, this assumption implies that all LA sites measured via Py-FTIR are active in the BVO reaction.

Other methods need to be evaluated to ascertain the absence of pore diffusion limitations such as altering (i) the particle size of the catalyst or (ii) the reaction temperature.[34,80] For the first method, HT Snβ consisting of larger particle sizes could be used. However, this strategy was deemed unsuitable as it could alter the nature of the active sites. This would complicate to attribute a change in catalytic activity entirely to pore diffusion limitations.

A better and simpler method is to decrease the reaction temperature since the reaction rate constant k is more temperature sensitive than the diffusion coefficient D. Both coefficients obey the exponential Arrhenius equation ($k = A \cdot e^{-Ea/RT}$ and $D = D_0 \cdot e^{-Ed/RT}$), but the effective activation energy E_a of the kinetic reaction lies in the range of 50 to 100 $kJ \cdot mol^{-1}$, in contrast to the activation energy of self-diffusion, which is below 50 $kJ \cdot mol^{-1}$.[81–84] Assuming that the catalytic activity plateaus at 93 $mM_{CL} \cdot h^{-1}$ due to pore diffusion limitations, we would expect the catalytic activity of the catalysts with the highest LA density to lie in the linear kinetic part upon lowering the temperature, as we force the catalytic reaction to take place at lower rate. However, as can be seen in Figure S16, when reducing the temperature to 60 °C, the graph retains an identical shape as Figure 6. A plateau is reached here at $r_{0,CL}$ of 25 $mM_{CL} \cdot h^{-1}$ for a similar LA density of 200 $\mu mol \cdot g^{-1}$. Since this initial formation rate lies in the linear part at 80 °C (Figure 6), we can conclude that the leveling off is not caused by pore diffusion limitations.

An alternative method for assessing (pore) diffusion limitations relies on calculating the effectiveness factor η as a function of the Thiele modulus ϕ.[85,86] The effectiveness factor η is defined as the ratio of the observed rate (R_e) to the intrinsic rate (R_b) in absence of mass and heat gradients (eq 5). By assuming that the pellet temperature is isothermal, the effectiveness factor η

can be expressed as the product of the pore and film effectiveness factors, η_{pore} and η_{film}, respectively (eq 6) with the Thiele modulus ϕ defined as the ratio of the intrinsic rate, calculated at bulk fluid phase conditions, to the maximum rate of effective diffusion at the external pellet surface. Considering the particles as a sphere with radius r_p, eq 7 is used with k as a reaction constant, c_b the bulk concentration, n the order of the reaction and D_e the effective diffusion. The η_{film} part of the equation is also influenced by the Biot number Bi_m (equation 8).[87] Since the BVO reaction obeys a first order rate[88], and as no film diffusion limitations occur (see part 1), eq 6 can be simplified to eq 9.

$$\eta = \frac{R_e}{R_b} \tag{5}$$

$$\eta = \eta_{pore}\,\eta_{film} = \frac{3}{\phi}\left(\frac{1}{\tanh(\phi)} - \frac{1}{\phi}\right) x \left(\frac{Bi_m \tanh(\phi)}{\phi + (Bi_m - 1)\tanh(\phi)}\right) \tag{6}$$

$$\phi = r_p\sqrt{\frac{k c_b^{n-1}}{D_e}} \tag{7}$$

$$Bi_m = \frac{k_f\, r_p}{D_e} \tag{8}$$

$$\eta = \eta_{pore} = \frac{3}{\phi}\left(\frac{1}{\tanh(\phi)} - \frac{1}{\phi}\right) \; with\; \phi = r_p\sqrt{\frac{k}{D_e}} \tag{9}$$

The parameters that influence pore diffusion in a first order reaction are r_p, k and D_e. The particle size of a commercial beta zeolite lies between 60-500 nm. [2,89–91] An average particle size of 500 nm was confirmed via SEM for 10Snβ-N_2/air (Figure S17), but because particles as large as 1 µm were also detected, we conservatively assumed the particle size to be 1 µm. The reaction constant k was estimated at 0.27 h^{-1} at 80 °C reaction temperature, which is the value for the most active catalyst (10Snβ-N_2/air, *vide infra*). The effective diffusion coefficient D_e of cyclohexanone in the β zeolite crystal was approximated using D_e values of similar compounds such as phenol and benzyl alcohol (Table S4). Even assuming a conservatively low D_e value of $1.5 \cdot 10^{-15}$ $m^2 \cdot s^{-1}$, the calculated effectiveness factor η_{pore} is still 1.

Both the temperature decrease approach presented above and the effectiveness factor η_{pore} of 1 suggest the absence of pore diffusion limitations. Therefore, the BVO reaction proceeds in the kinetic regime for the most active Sn catalysts, and the activity plateau is therefore caused by another phenomenon.

To get further insights into the difference between the active sites, a kinetic study was performed on the BVO reaction. Key kinetic parameters such as the apparent activation energy (E_a) and pre-exponential factor (k_0) were determined by varying the temperature between 50 and 80 °C. The Arrhenius plots for the different Snβ catalysts are displayed in Figure S18A. Apparent E_a values were obtained from the slopes of these plots, whereas k_0 values were derived from the calculated intercept with the y-axis; values are listed in Table 2. All catalysts show a comparable apparent E_a (between 70.1 and 71.3 kJ·mol^{-1}). Such E_a values confirm again the absence of mass transfer limitations for the catalysts used in this work. Since the amount of active sites is accounted for in the k_0, as expected, the k_0 values of air-calcined catalysts increase with higher Sn content. Initially the same happens for the N_2/air- samples up to 5 wt % when a plateau is reached. The pre-exponential factor k_0 is strongly correlated with the entropic factor which can be calculated through the Eyring plots.[92] The calculated enthalpic ($\Delta H^{\ddagger}$) and entropic ($\Delta S^{\ddagger}$) values of the transition states are presented in Table 2.

Table 2. Apparent Activation Energy (E_a), Pre-exponential Factor (k_0), Enthalpy ($\Delta H^{\ddagger}$) and Entropy ($\Delta S^{\ddagger}$) for the Bimolecular BVO Reaction with Different Snβ Catalysts

Catalyst	E_a (kJ·mol^{-1})	k_0 (h^{-1})	$\Delta H^{\ddagger}$ (kJ·mol^{-1})	$\Delta S^{\ddagger}$ (J·mol^{-1}·K^{-1})
5Snβ-air	70.6	2.30 10^9	67.8	-143.1
10Snβ-air	70.1	4.53 10^9	67.3	-137.5
1Snβ-N_2/air	70.6	1.39 10^9	67.8	-147.5
2Snβ-N_2/air	70.8	2.93 10^9	68.0	-141.1
5Snβ-N_2/air	71.2	8.77 10^9	68.4	-132.0
7Snβ-N_2/air	71.3	8.75 10^9	68.5	-132.0
10Snβ-N_2/air	70.6	7.43 10^9	67.8	-133.4

For all materials, a transition state with a similar enthalpic level is formed during BVO reaction at the Sn active site. The highly negative activation entropies are typical for associative processes and indicate the formation of a more ordered transition state complex – in this case, the Criegee

intermediate.[93] Initially, the entropic factor ($\Delta S^{\ddagger}$) correlates with the LA density until it levels off at 200 µmol·g^{-1} (Figure 8).

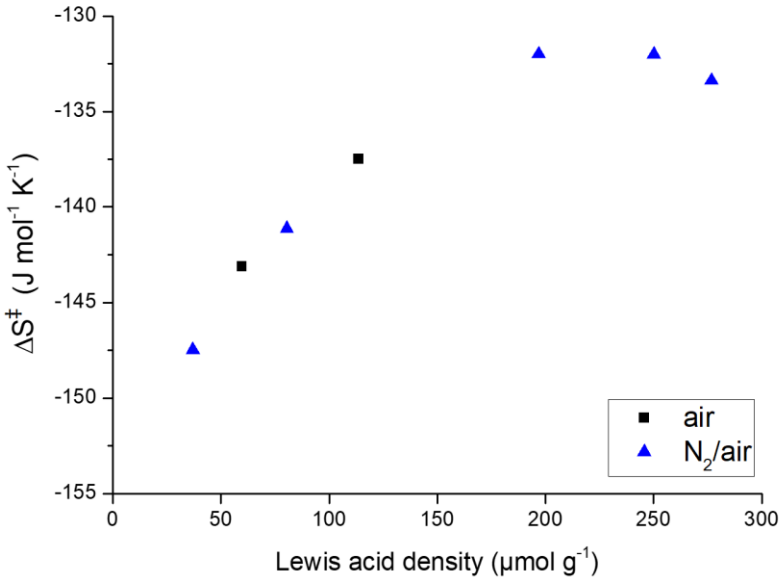

Figure 8. Entropic factor ($\Delta S^{\ddagger}$) as a function of LA density (µmol·g^{-1}) for Snβ-(N_2/)air zeolites (air: black squares, N_2/air: blue triangles). The Lewis acid density was calculated by Py-FTIR at 150 °C and 1.42 cm·µmol^{-1} as integrated molar extinction coefficient.[59] The enthalpic factor ($\Delta S^{\ddagger}$) was derived from the calculated intercept with the y-axis of the respective Eyring plot.

The $\Delta S^{\ddagger}$ factor is influenced by (i) the change in entropies of transition state structures and (ii) the relative abundance of active Sn sites.[94] Hence, the increase in $\Delta S^{\ddagger}$ up to LA density of 200 µmol·g^{-1} correlates with the increased amount of LA Sn sites. Above 200 µmol·g^{-1}, the activity per Sn decreases (as visualized by TOF, Figure S12). It could be that, at higher metal loadings, Sn is incorporated in T-sites which are in very close proximity to each other. These sites are still accessible to the probe pyridine in FTIR. However, the bimolecular BVO reaction requires an adequate orientation of both cyclohexanone and H_2O_2 with a single Sn site. Hence, it is very plausible that two proximate neighboring sites cannot be active simultaneously.

To investigate this hypothesis, we checked the accessibility of the LA sites of the catalysts with a larger probe molecule, namely 2,6-lutidine (Lu).[95] If the LA sites (above 200 µmol·g^{-1}, measured via Py) are in too close proximity, the Sn sites cannot be reached separately, thus, the ratio of the adsorbed Lu to adsorbed Py (Lu/Py-ratio) should be lower compared to a catalyst with a lower LA density (< 200 µmol·g^{-1}) in which the Sn sites will be less proximate. Therefore, we tested 10Snβ-

air and 10Snβ-N_2/air catalysts having a (Py-calculated) LA density of 114 and 277 μmol·g^{-1}, respectively. The FTIR spectrum of Lu adsorbed on 10Snβ-air is provided in Figure S19. The contribution at 1612 cm^{-1} is assigned to coordinated Lu species on LA sites.[95] The LA density was calculated from the spectra (see details in Materials and Methods) by using the molar extinction coefficient of 3.4 cm.μmol^{-1}, determined by Onfroy et al.[96] The calculated Lu/Py ratios were found very similar; 0.30 and 0.33 for 10Snβ-air and 10Snβ-N_2/air, respectively, indicating that the active site proximity hypothesis seems unlikely.

The accessibility hypothesis was further investigated by performing the BVO reaction with smaller substrates. By reducing the substrate size, one could expect that potential accessibility issues are less pronounced, hence overcoming the activity plateau at high LA density. However, a similar profile was apparent when performing the reaction with cyclobutanone (Figure S20A) and cyclopentanone (Figure S20B). These results further corroborate that accessibility of the Sn sites is not the main reason for the activity plateau.

Instead, the plateau could arise from the additional Sn that is incorporated in the less favorable T-sites at high Sn loadings. As the pre-exponential factor k_0 is influenced by both content and reaction efficiency of the active Sn sites, this can be investigated by eliminating the content factor. In Figure S18B, a modified Arrhenius plot is presented wherein the *k*-values are divided by the specific LA density (abbreviated as LAD). Next, the calculated $\left(\frac{k}{\mathrm{LAD}}\right)_0$-values, derived from the intercept of Figure S18B, are plotted in Figure 9 as function of LA density (measured via Py-FTIR). The active Sn sites have approximately the same reaction efficiency for the BVO reaction up to a LA density of 200 μmol g^{-1}. A further increase in amount of LA sites decreases the average reaction efficiency of the Sn sites.

Hence, we conclude that for the BVO, a maximum activity can be obtained at a LA density of 200 μmol·g^{-1}. Increasing the Sn content beyond a LA density of 200 μmol·g^{-1} yields no benefit since the average reaction efficiency of the active sites reduces due to the incorporation of Sn in less favorable sites.

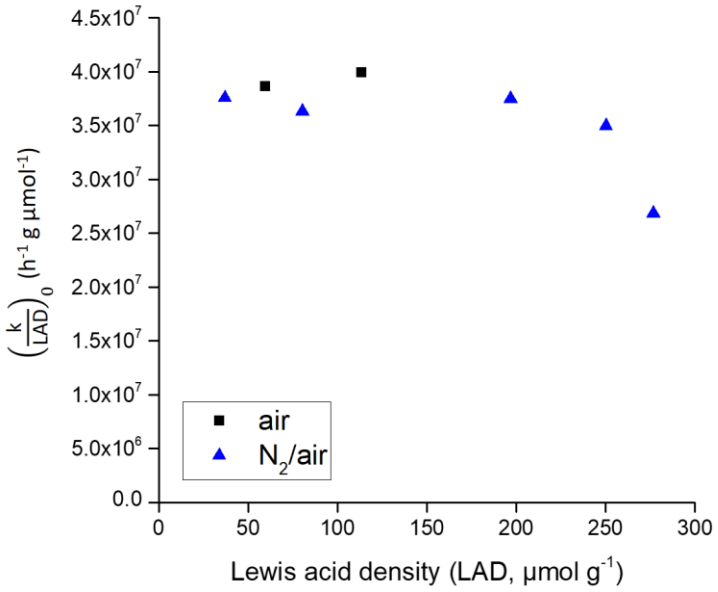

Figure 9. $\left(\frac{k}{\mathrm{LAD}}\right)_0$-values as a function of Lewis acid density (LAD). $\left(\frac{k}{\mathrm{LAD}}\right)_0$ is determined via the intercept of the modified Arrhenius plot, wherein the reaction constant *k* is divided by the Lewis acid density of the specific catalyst.

Conclusion

A fast, efficient and established procedure to obtain β zeolites with Lewis acidic Sn sites is via SSI of Sn. The thermal treatment during SSI is crucial to obtain highly active Snβ catalysts. However, the influence of rather trivial parameters such as heating atmosphere on the formation of active Sn sites, and the mechanisms at play are often overlooked.

In this paper, we elucidated the mechanistic role of the pre-pyrolysis step during SSI on the structure and activity of the resulting Snβ catalysts. The significantly higher catalytic activity of Snβ catalysts treated by inert heating was confirmed for the H_2O_2-mediated Baeyer-Villiger oxidation reaction. Extensive solid-state characterization of these Snβ catalysts by N_2-physisorption, PXRD, DRUV-vis, FTIR, XPS, and ^{119}Sn Mössbauer spectroscopy revealed an improved framework Sn incorporation, and hence a higher Sn dispersion.

The higher Sn dispersion can be explained by a difference in Sn-oxidation state during heat treatment as confirmed by *in situ* TPDE-MS, TGA and ^{119}Sn Mössbauer spectroscopy. In an inert atmosphere, Sn(II)O species instead of Sn(IV)O_2 are *in situ* generated during high-temperature

zeolite-associated Sn(II) acetate decomposition. It was rationalized that such *in situ*-generated Sn(II)O species play a key role in creating Snβ catalysts with high Sn dispersion because of their higher volatility, hence mobility, and thus increased probability to encounter silanol nests.

Finally, we established the crucial link between the features of the catalyst and its activity. Irrespective of the heat treatment applied, a positive linear relationship was seen between the catalytic activity for the BVO reaction and the LA density up to 200 $\mu mol \cdot g^{-1}$. At a higher LA density, the activity plateaued. This activity plateau was not due to diffusion limitations, since they were excluded by (i) lowering the reaction temperature, (ii) calculating the effectiveness factor η and (iii) performing a kinetic analysis. Instead, it seems that at high Sn loadings, additional Sn becomes incorporated in less favorable T-sites which are less efficient in the bimolecular BVO reaction. As a result, the highest catalytic activity for the Snβ-catalyzed BVO reaction is obtained at a LA density of 200 $\mu mol \cdot g^{-1}$. Further increasing the Sn content beyond this LA density yields no additional benefit.

MATERIALS AND METHODS

Catalyst synthesis

A calcined commercial Al-β (CP814c, Zeolyst International, SiO_2/Al_2O_3 = 38) was dealuminated by stirring the zeolite powder for 20 h in a 65% nitric acid solution (20 $mL \cdot g^{-1}$ of zeolite) at 100 °C. Afterwards, the solids were filtered and washed thoroughly with water and dried overnight at 60 °C. The post-synthesis procedures were preceded by an activation of the dealuminated zeolite at 150 °C to remove any physisorbed water. The procedure of Hammond was followed for the solid state synthesis with Sn(II) Acetate.[38,39] The appropriate amount of Sn precursor was added to the dealuminated β and manually ground for 10 min in a pestle and mortar. Two calcination procedure were used. In this first method, the sample was heated under static air in a muffle furnace to 550 °C (2 $°C \cdot min^{-1}$) for 6 h. In the second method, the sample was heated in a quartz tube inside a tubular oven to 550 °C (2 $°C \cdot min^{-1}$) first in a N_2-flow (3 h) and subsequently in an air-flow (3 h) (Figure S1). Gas flow rates of 20$mL \cdot min^{-1}$ were employed.

We also checked if the air-flow parameter affected the outcome of catalytic activity since we used static air (muffle-furnace) in the first calcination method and an N_2 and air flow in the second method. However, no effect of the air-flow parameter was observed.

Characterization Techniques

Powder XRD (PXRD) patterns were recorded on a high-throughput STOE Stadi P Combi diffractometer in the transmission mode equipped with Cu- $K\alpha_1$ source and IP-PSD detector. To calculate the crystallite size of SnO_2 present in the samples, the Debye-Scherrer equation was used:

$$d = \frac{k\lambda}{\beta \cos\theta} \qquad (10)$$

With d the crystallite size, λ the wavelength of the X-ray radiation (Cu- $K\alpha_1$ = 0.15406 nm), constant k of 0.9, β is the full width at half maximum height in radians (FWHM) and θ is the diffraction angle in radians. To estimate the average crystallite size of SnO_2, the two most intense, indexed peaks, (101) and (211) at 33.9 and 52.3°, respectively, were used.[44,45]

TGA of the samples was performed on TA Instruments TGA Q500. About 8 mg of the ground Sn(II) acetate and deAlβ mixture (with a final Sn-content of 5 wt %) was heated at 2 °C·min^{-1} to 550 °C in O_2 or N_2 and kept isothermal for 6 h (6 h in O_2 or 3 h in N_2 followed by 3 h in O_2) at a flow rate of 90 mL·min^{-1}.

TPDE MS analysis was performed in a horizontal home-made oven with temperature control, coupled to a Pfeiffer Omnistar Mass spectrometer. Sn(II) acetate and deAlβ (5 wt % Sn) were ground for 10 minutes and 200 mg was pelletized and placed inside the quartz tube. The sample was heated at 2 °C·min^{-1} in 20 ml·min^{-1} of an inert atmosphere (He-flow) or oxidizing flow (O_2-flow) to 550 °C. m/z of 18, 44, 45 and 58 were tracked with the MS to follow the production of water, CO_2, acetic acid and acetone, respectively.

N_2 sorption measurements were performed using a Micromeritics Instruments Tristar 3000 at 77 K. Samples were degassed under N_2-flow at 300 °C for 6 h prior to measurement. The relative nitrogen pressure was varied between 0.01 and 0.99 (p/p_0). The specific surface area was calculated using the Brunauer–Emmett–Teller (BET) theory, and pore volumes were calculated by the t-plot method.

DRUV-vis measurements were performed in quartz U-tubes equipped with a window. The samples were dried at 550 °C for 1 h in an air-flow inside the tubes and measured, after cooling, on an Agilent Cary 5000 spectrophotometer. Dried barium sulfate was used as the diffuse reflectance standard.

Elemental analysis was performed using an ICP-AES (Perkin Elmer Optima 3300 DV) with signals for Sn, Al, and Si at 189.9, 238.2, and 251.6 nm, respectively. Before ICP-AES, the samples were decomposed with lithium metaborate at 1000 °C and dissolved in 5% HCl in Milli-Q water.

FTIR measurements were performed on a Nicolet 6700 Spectrometer equipped with DTGS detector. Samples were pressed into self-supporting wafers and degassed at 400 °C *in vacuo* for 1 h before measurements. LA sites were analyzed with gas-phase pyridine, lutidine or deuterated acetonitrile. 2,6-Lutidine was adsorbed at 50 °C, by exposing the sample to 8 mbar of probe molecule until saturation. Spectra were recorded at 150 °C *in vacuo* after 15 min of equilibration and 3.4 $cm \cdot \mu mol^{-1}$ was used as integrated molar extinction coefficient for calculations of LA density at 1612 cm^{-1}.[96] For pyridine adsorption, the samples were subjected to 20 mbar of the probe until saturation at 50 °C. Spectra were recorded at 150 °C *in vacuo* after equilibration for 40 min. 1.42 $cm \cdot \mu mol^{-1}$ was used as integrated molar extinction coefficient for calculations of LA density at 1451 cm^{-1}.[59] Deuterated acetonitrile was adsorbed at 30 °C. The samples were exposed to sequential doses of 4 mbar of probe molecule until saturation, which was evidenced when gas-phase CD_3CN (2267 cm^{-1}) appeared. Once saturated, a spectrum was recorded at 30 °C after 30 s *in vacuo*. The spectra were deconvoluted in open Sn sites (2316 cm^{-1}), closed Sn sites (2308 cm^{-1}), SnO_2 (2287 cm^{-1}), silanol groups (2275 cm^{-1}), and physisorbed or gas-phase CD_3CN (2265 cm^{-1}) with OMNIC software. All peaks were fitted using mixed Gaussian-Lorentzian peaks (50/50) except for the peak corresponding to physisorbed CD_3CN, which was fitted using a fully Lorentzian (0/100) peak. For all deconvolutions, a peak centers variation of ± 3 cm^{-1} was allowed and FWHM values ranged from 5- 20 cm^{-1}.[22] For open and closed Sn sites, integrated molar extinction coefficient of 1.04 and 2.04, respectively, were used.[59]

For all probe molecules, spectra of unloaded materials were recorded as reference spectra. The number of LA sites titrated by the probe molecules was calculated using the following equation.

$$\text{LA density } (\mu mol \cdot g^{-1}) = \frac{\text{integrated peak area } (cm^{-1})}{\text{molar extinction coefficient } (cm\ \mu mol^{-1})} \times \frac{A_{wafer}\ (cm^2)}{m\ (g)} \quad (11)$$

With A_{wafer} and m the area and the mass of the dry wafer, respectively.

XPS measurements were carried out on a SSI X probe spectrometer (model SSI 100, Surface Science Laboratories, Mountain View, CA) equipped with a monochromatized Al-Kα radiation (1486 eV). The sample powders, pressed in small stainless troughs of 4 mm diameter, were placed on an insulating home-made ceramic carousel. The pressure in the analysis chamber was around 10^{-6} Pa. The analyzed area was ~1.4 mm^2 and the pass energy was set at 150 eV. The Si2p peak of silicon was fixed to 103.5 eV to set the binding energy scale. Data treatment was performed with the CasaXPS program (Casa Software Ltd, UK); spectra were decomposed with the least

squares fitting routine provided by the software with a Gaussian/Lorentzian (85/15) product function and after baseline was subtracted.

^{119}Sn Mössbauer spectra of the powder samples were collected at RT and 77 K in transmission geometry, using a constant-acceleration Mössbauer spectrometer equipped with a $Ca^{119m}SnO_3$ source kept at RT and a variable-temperature (Thor Cryogenics) liquid nitrogen bath cryostat. The spectrometer was calibrated with metallic iron at room temperature and 77 K. Analyses of the spectra were performed by the IMSG code using Lorentzian-type lines.[97] The sample treated in inert conditions was stored, sealed and transported in N_2-atmosphere and the corresponding Mössbauer sample holder was prepared and sealed in a glovebox under N_2-atmosphere prior to its measurement.

Catalytic Reactions

Baeyer-Villiger oxidation (BVO) reactions were performed in magnetically stirred thick-walled glass reactors, capped with a rubber stopper and placed in a temperature controlled copper block. The reaction was conducted at 80 °C (or as mentioned), 10 mg of catalyst was added to 330 mM of cyclohexanone in 5 mL of 1,4-dioxane. The glass reactor was heated to the required temperature for 10 min, prior to the addition of 50 wt % H_2O_2 in an H_2O_2/ketone ratio of 1.5. Biphenyl was used as internal standard for chromatographic analysis. Reaction conditions of the BV oxidation of cyclopentanone are identical to the reaction with cyclohexanone at 80°C. For cyclobutanone, following reaction conditions were used: H_2O_2/ketone ratio = 1.5 (50wt% H_2O_2); c_{ketone} = 330 mM; 10 mg catalyst in 7.5 mL dioxane at 20 °C.

To determine the initial formation rate, samples were taken at regular time intervals and filtered to remove the catalysts. Samples used for the calculation of the initial formation rate contained a CL-yield below 10%. MnO_2 powder was added to the aliquots to decompose H_2O_2, which is still present in a large amount and is detrimental for the GC-column. After decomposition of H_2O_2 to O_2 and H_2O, MnO_2 powder was removed by filtering and the aliquots were quantitatively analyzed on a Hewlett Packard HP 6890 GC equipped with an HP 7683 autosampler, a 30m CP-wax-52 CB column and a FID detector. Identification of products was based on retention time analysis.

Apparent activation energy (E_a), pre-exponential factor (k_0), enthalpy ($\Delta H^{\ddagger}$) and entropy ($\Delta S^{\ddagger}$) for the bimolecular BVO reaction were calculated via following equations:

Arrhenius equation: $\ln k = \ln k_0 - \frac{E_a}{R} \cdot \frac{1}{T}$ (12)

Eyring Equation: $\ln\frac{k}{T} = \frac{-\Delta H^{\ddagger}}{R}\cdot\frac{1}{T} + \ln\frac{k_B}{h} + \frac{\Delta S^{\ddagger}}{R}$ (13)

With the gas constant R, Boltzmann constant k_B and Planck constant h.

ASSOCIATED CONTENT

Supporting information

The following files are available free of charge.

Catalytic activity: kinetic plots, assessment of film diffusion limitations, catalytic activity at 60°C, BVO with different substrates (butyrolactone and valerolactone), published results of catalytic activity of 2-adamantanone oxidation, (modified) Arrhenius plots, catalytic activity against open and closed Sn-sites and TOF against LA density.

Catalyst characterization: DRUV-vis spectra and deconvolution, XPS results, ^{119}Sn Mössbauer spectra, FTIR spectra (Pyridine, CD_3CN and 2,6 Lutidine), TPDE-MS and TGA profiles, SEM image, physicochemical properties of Snβ catalysts, extraframework/framework Sn-ratio and normalized silanol area of Snβ catalysts, ^{119}Sn Mössbauer values, and the reported effective diffusivity in beta zeolites.

AUTHOR INFORMATION

Corresponding Authors

*E-mail: michiel.dusselier@kuleuven.be

*E-mail: bert.sels@kuleuven.be

Author Contributions

The manuscript was written through contributions of all authors. All authors have given approval to the final version of the manuscript.

Notes

The authors declare no competing financial interest.

ACKNOWLEDGMENTS

M.D. and B.S. thank FWO for the SB PhD fellowship (grant 1S96018N) to E.P. I.K. acknowledges FWO (grant 1260321N) for financial support. G.P. acknowledges VLAIO for financial support (Catalisti-SBO project SPICY). D.P.D. thanks the Francqui Foundation for his Francqui Research Professor chair. We are grateful to G. Ivanushkin for SEM-measurements.

REFERENCES

(1) Corma, A.; García, H. Lewis Acids as Catalysts in Oxidation Reactions: From Homogeneous to Heterogeneous Systems. *Chem. Rev.* **2002**, *102* (10), 3837–3892. https://doi.org/10.1021/cr010333u.

(2) Ferrini, P.; Dijkmans, J.; Clercq, R. De; de Vyver, S. Van; Dusselier, M.; Jacobs, P. A.; Sels, B. F. Lewis Acid Catalysis on Single Site Sn Centers Incorporated into Silica Hosts. *Coord. Chem. Rev.* **2017**, *343* (Supplement C), 220–255. https://doi.org/https://doi.org/10.1016/j.ccr.2017.05.010.

(3) Ennaert, T.; Aelst, J. Van; Dijkmans, J.; Clercq, R. De; Schutyser, W.; Dusselier, M.; Verboekend, D.; Sels, B. F. Potential and Challenges of Zeolite Chemistry in the Catalytic Conversion of Biomass. *Chem. Soc. Rev.* **2016**, *45*, 584–611. https://doi.org/10.1039/C5CS00859J.

(4) Li, Y.; Li, L.; Yu, J. Applications of Zeolites in Sustainable Chemistry. *Chem* **2017**, *3* (6), 928–949. https://doi.org/https://doi.org/10.1016/j.chempr.2017.10.009.

(5) Dijkmans, J.; Gabriels, D.; Dusselier, M.; de Clippel, F.; Vanelderen, P.; Houthoofd, K.; Malfliet, A.; Pontikes, Y.; Sels, B. F. Productive Sugar Isomerization with Highly Active Sn in Dealuminated Beta Zeolites. *Green Chem.* **2013**, *15* (10), 2777–2785. https://doi.org/10.1039/C3GC41239C.

(6) Moliner, M.; Román-Leshkov, Y.; Davis, M. E. Tin-Containing Zeolites Are Highly Active Catalysts for the Isomerization of Glucose in Water. *Proc. Natl. Acad. Sci. U. S. A.* **2010**, *107* (14), 6164–6168. https://doi.org/10.1073/pnas.1002358107.

(7) Román-Leshkov, Y.; Moliner, M.; Labinger, J. A.; Davis, M. E. Mechanism of Glucose Isomerization Using a Solid Lewis Acid Catalyst in Water. *Angew. Chemie Int. Ed.* **2010**,

49 (47), 8954–8957. https://doi.org/10.1002/anie.201004689.

(8) Bermejo-Deval, R.; Orazov, M.; Gounder, R.; Hwang, S.-J.; Davis, M. E. Active Sites in Sn-Beta for Glucose Isomerization to Fructose and Epimerization to Mannose. *ACS Catal.* **2014**, *4* (7), 2288–2297. https://doi.org/10.1021/cs500466j.

(9) Choudhary, V.; Pinar, A. B.; Sandler, S. I.; Vlachos, D. G.; Lobo, R. F. Xylose Isomerization to Xylulose and Its Dehydration to Furfural in Aqueous Media. *ACS Catal.* **2011**, *1* (12), 1724–1728. https://doi.org/10.1021/cs200461t.

(10) Lew, C. M.; Rajabbeigi, N.; Tsapatsis, M. Tin-Containing Zeolite for the Isomerization of Cellulosic Sugars. *Microporous Mesoporous Mater.* **2012**, *153*, 55–58. https://doi.org/https://doi.org/10.1016/j.micromeso.2011.12.020.

(11) Hwang, S.-J.; Gounder, R.; Bhawe, Y.; Orazov, M.; Bermejo-Deval, R.; Davis, M. E. Solid State NMR Characterization of Sn-Beta Zeolites That Catalyze Glucose Isomerization and Epimerization. *Top. Catal.* **2015**, *58* (7), 435–440. https://doi.org/10.1007/s11244-015-0388-7.

(12) Botti, L.; Meier, S.; Hammond, C. Mechanistic Studies of Continuous Glucose Upgrading over Lewis Acidic Silicates by Operando UV–Vis and HSQC NMR. *ACS Catal.* **2021**, 1296–1308. https://doi.org/10.1021/acscatal.0c03638.

(13) Botti, L.; Navar, R.; Tolborg, S.; Martinez-Espin, J. S.; Padovan, D.; Taarning, E.; Hammond, C. Influence of Composition and Preparation Method on the Continuous Performance of Sn-Beta for Glucose-Fructose Isomerisation. *Top. Catal.* **2019**, *62* (17), 1178–1191. https://doi.org/10.1007/s11244-018-1078-z.

(14) Padovan, D.; Botti, L.; Hammond, C. Active Site Hydration Governs the Stability of Sn-Beta during Continuous Glucose Conversion. *ACS Catal.* **2018**, *8* (8), 7131–7140. https://doi.org/10.1021/acscatal.8b01759.

(15) Holm, M. S.; Saravanamurugan, S.; Taarning, E. Conversion of Sugars to Lactic Acid Derivatives Using Heterogeneous Zeotype Catalysts. *Science (80-.).* **2010**, *328* (5978), 602–605. https://doi.org/10.1126/science.1183990.

(16) Orazov, M.; Davis, M. E. Tandem Catalysis for the Production of Alkyl Lactates from Ketohexoses at Moderate Temperatures. *Proc. Natl. Acad. Sci.* **2015**, *112* (38), 11777–11782. https://doi.org/10.1073/pnas.1516466112.

(17) Tang, B.; Li, S.; Song, W.-C.; Yang, E.-C.; Zhao, X.-J.; Guan, N.; Li, L. Fabrication of Hierarchical Sn-Beta Zeolite as Efficient Catalyst for Conversion of Cellulosic Sugar to Methyl Lactate. *ACS Sustain. Chem. Eng.* **2020**, *8* (9), 3796–3808. https://doi.org/10.1021/acssuschemeng.9b07061.

(18) Van de Vyver, S.; Odermatt, C.; Romero, K.; Prasomsri, T.; Román-Leshkov, Y. Solid Lewis Acids Catalyze the Carbon–Carbon Coupling between Carbohydrates and Formaldehyde. *ACS Catal.* **2015**, *5* (2), 972–977. https://doi.org/10.1021/cs5015964.

(19) Lewis, J. D.; de Vyver, S.; Román-Leshkov, Y. Acid–Base Pairs in Lewis Acidic Zeolites Promote Direct Aldol Reactions by Soft Enolization. *Angew. Chemie Int. Ed.* **2015**, *54* (34), 9835–9838. https://doi.org/10.1002/anie.201502939.

(20) Corma, A.; Domine, M. E.; Nemeth, L.; Valencia, S. Al-Free Sn-Beta Zeolite as a Catalyst for the Selective Reduction of Carbonyl Compounds (Meerwein−Ponndorf−Verley Reaction). *J. Am. Chem. Soc.* **2002**, *124* (13), 3194–3195. https://doi.org/10.1021/ja012297m.

(21) Dijkmans, J.; Schutyser, W.; Dusselier, M.; Sels, B. F. Snβ-Zeolite Catalyzed Oxido-Reduction Cascade Chemistry with Biomass-Derived Molecules. *Chem. Commun.* **2016**, *52* (40), 6712–6715. https://doi.org/10.1039/C6CC00199H.

(22) Di Iorio, J. R.; Johnson, B. A.; Román-Leshkov, Y. Ordered Hydrogen-Bonded Alcohol Networks Confined in Lewis Acid Zeolites Accelerate Transfer Hydrogenation Turnover Rates. *J. Am. Chem. Soc.* **2020**, *142* (45), 19379–19392. https://doi.org/10.1021/jacs.0c09825.

(23) Qi, G.; Chu, Y.; Wang, Q.; Wang, X.; Li, Y.; Trébosc, J.; Lafon, O.; Xu, J.; Deng, F. Gem-Diol-Type Intermediate in the Activation of a Ketone on Sn-β Zeolite as Studied by Solid-State NMR Spectroscopy. *Angew. Chemie Int. Ed.* **2020**, *59* (44), 19532–19538. https://doi.org/10.1002/anie.202005589.

(24) Corma, A.; Nemeth, L. T.; Renz, M.; Valencia, S. Sn-Zeolite Beta as a Heterogeneous Chemoselective Catalyst for Baeyer–Villiger Oxidations. *Nature* **2001**, *412*, 423.

(25) Yakabi, K.; Milne, K.; Buchard, A.; Hammond, C. Selectivity and Lifetime Effects in Zeolite-Catalysed Baeyer–Villiger Oxidation Investigated in Batch and Continuous Flow. *ChemCatChem* **2016**, *8* (22), 3490–3498. https://doi.org/10.1002/cctc.201600955.

(26) Yakabi, K.; Mathieux, T.; Milne, K.; López-Vidal, E. M.; Buchard, A.; Hammond, C. Continuous Production of Biorenewable, Polymer-Grade Lactone Monomers through Sn-β-Catalyzed Baeyer-Villiger Oxidation with H 2 O 2. *ChemSusChem* **2017**, *10* (18), 3652–3659. https://doi.org/10.1002/cssc.201701298.

(27) Schutyser, W.; den Bosch, S.; Dijkmans, J.; Turner, S.; Meledina, M.; Van Tendeloo, G.; Debecker, D. P.; Sels, B. F. Selective Nickel-Catalyzed Conversion of Model and Lignin-Derived Phenolic Compounds to Cyclohexanone-Based Polymer Building Blocks. *ChemSusChem* **2015**, *8* (10), 1805–1818. https://doi.org/10.1002/cssc.201403375.

(28) Luo, H. Y.; Lewis, J. D.; Román-Leshkov, Y. Lewis Acid Zeolites for Biomass Conversion: Perspectives and Challenges on Reactivity, Synthesis, and Stability. *Annu. Rev. Chem. Biomol. Eng.* **2016**, *7* (1), 663–692. https://doi.org/10.1146/annurev-chembioeng-080615-034551.

(29) Tolborg, S.; Katerinopoulou, A.; Falcone, D. D.; Sádaba, I.; Osmundsen, C. M.; Davis, R. J.; Taarning, E.; Fristrup, P.; Holm, M. S. Incorporation of Tin Affects Crystallization, Morphology, and Crystal Composition of Sn-Beta. *J. Mater. Chem. A* **2014**, *2* (47), 20252–20262. https://doi.org/10.1039/C4TA05119J.

(30) Hammond, C.; Padovan, D.; Tarantino, G. Porous Metallosilicates for Heterogeneous, Liquid-Phase Catalysis: Perspectives and Pertaining Challenges. *R. Soc. Open Sci.* **2018**, *5* (2), 171315. https://doi.org/10.1098/rsos.171315.

(31) Chang, C.-C.; Wang, Z.; Dornath, P.; Je Cho, H.; Fan, W. Rapid Synthesis of Sn-Beta for the Isomerization of Cellulosic Sugars. *RSC Adv.* **2012**, *2* (28), 10475–10477. https://doi.org/10.1039/C2RA21381H.

(32) Kang, Z.; Zhang, X.; Liu, H.; Qiu, J.; Yeung, K. L. A Rapid Synthesis Route for Sn-Beta Zeolites by Steam-Assisted Conversion and Their Catalytic Performance in Baeyer–Villiger Oxidation. *Chem. Eng. J.* **2013**, *218*, 425–432. https://doi.org/https://doi.org/10.1016/j.cej.2012.12.019.

(33) Hammond, C. Chapter 15 - Sn-Substituted Zeolites as Heterogeneous Catalysts for Liquid-Phase Catalytic Technologies. In *Morphological, Compositional, and Shape Control of Materials for Catalysis*; Fornasiero, P., Cargnello, M., Eds.; Studies in Surface Science and Catalysis; Elsevier, 2017; Vol. 177, pp 567–611. https://doi.org/https://doi.org/10.1016/B978-0-12-805090-3.00015-2.

(34) Li, P.; Liu, G.; Wu, H.; Liu, Y.; Jiang, J.; Wu, P. Postsynthesis and Selective Oxidation Properties of Nanosized Sn-Beta Zeolite. *J. Phys. Chem. C* **2011**, *115* (9), 3663–3670. https://doi.org/10.1021/jp1076966.

(35) Jin, J.; Ye, X.; Li, Y.; Wang, Y.; Li, L.; Gu, J.; Zhao, W.; Shi, J. Synthesis of Mesoporous Beta and Sn-Beta Zeolites and Their Catalytic Performances. *Dalt. Trans.* **2014**, *43* (22), 8196–8204. https://doi.org/10.1039/C4DT00567H.

(36) Dijkmans, J.; Demol, J.; Houthoofd, K.; Huang, S.; Pontikes, Y.; Sels, B. Post-Synthesis Snβ: An Exploration of Synthesis Parameters and Catalysis. *J. Catal.* **2015**, *330*, 545–557. https://doi.org/10.1016/j.jcat.2015.06.023.

(37) Vega-Vila, J. C.; Harris, J. W.; Gounder, R. Controlled Insertion of Tin Atoms into Zeolite Framework Vacancies and Consequences for Glucose Isomerization Catalysis. *J. Catal.* **2016**, *344*, 108–120. https://doi.org/https://doi.org/10.1016/j.jcat.2016.09.011.

(38) Hammond, C.; Conrad, S.; Hermans, I. Simple and Scalable Preparation of Highly Active Lewis Acidic Sn-β. *Angew. Chemie Int. Ed.* **2012**, *51* (47), 11736–11739. https://doi.org/10.1002/anie.201206193.

(39) Hammond, C.; Padovan, D.; Al-Nayili, A.; Wells, P. P.; Gibson, E. K.; Dimitratos, N. Identification of Active and Spectator Sn Sites in Sn-β Following Solid-State Stannation, and Consequences for Lewis Acid Catalysis. *ChemCatChem* **2015**, *7* (20), 3322–3331. https://doi.org/10.1002/cctc.201500545.

(40) Hu, W.; Wan, Y.; Zhu, L.; Cheng, X.; Wan, S.; Lin, J.; Wang, Y. A Strategy for the Simultaneous Synthesis of Methallyl Alcohol and Diethyl Acetal with Sn-β. *ChemSusChem* **2017**, *10* (23), 4715–4724. https://doi.org/10.1002/cssc.201701435.

(41) Boronat, M.; Corma, A.; Renz, M.; Sastre, G.; Viruela, P. M. A Multisite Molecular Mechanism for Baeyer–Villiger Oxidations on Solid Catalysts Using Environmentally Friendly H2O2 as Oxidant. *Chem. – A Eur. J.* **2005**, *11* (23), 6905–6915. https://doi.org/10.1002/chem.200500184.

(42) Madon, R. J.; Boudart, M. Experimental Criterion for the Absence of Artifacts in the Measurement of Rates of Heterogeneous Catalytic Reactions. *Ind. Eng. Chem. Fundam.* **1982**, *21* (4), 438–447. https://doi.org/10.1021/i100008a022.

(43) Dijkmans, J.; Dusselier, M.; Gabriëls, D.; Houthoofd, K.; Magusin, P. C. M. M.; Huang, S.; Pontikes, Y.; Trekels, M.; Vantomme, A.; Giebeler, L.; Oswald, S.; Sels, B. F. Cooperative Catalysis for Multistep Biomass Conversion with Sn/Al Beta Zeolite. *ACS Catal.* **2015**, *5* (2), 928–940. https://doi.org/10.1021/cs501388e.

(44) Uvarov, V.; Popov, I. Metrological Characterization of X-Ray Diffraction Methods for Determination of Crystallite Size in Nano-Scale Materials. *Mater. Charact.* **2007**, *58* (10), 883–891. https://doi.org/https://doi.org/10.1016/j.matchar.2006.09.002.

(45) Aziz, M.; Abbas, S. S.; Baharom, W. R. W.; Mahmud, W. Z. W. Structure of SnO2 Nanoparticles by Sol–Gel Method. *Mater. Lett.* **2012**, *74*, 62–64. https://doi.org/https://doi.org/10.1016/j.matlet.2012.01.073.

(46) Bermejo-Deval, R.; Gounder, R.; Davis, M. E. Framework and Extraframework Tin Sites in Zeolite Beta React Glucose Differently. *ACS Catal.* **2012**, *2* (12), 2705–2713. https://doi.org/10.1021/cs300474x.

(47) Joshi, H.; Ochoa-Hernández, C.; Nürenberg, E.; Kang, L.; Wang, F. R.; Weidenthaler, C.; Schmidt, W.; Schüth, F. Insights into the Mechanochemical Synthesis of Sn-β: Solid-State Metal Incorporation in Beta Zeolite. *Microporous Mesoporous Mater.* **2020**, 110566. https://doi.org/https://doi.org/10.1016/j.micromeso.2020.110566.

(48) Omegna, A.; Vasic, M.; van Bokhoven, J.; Pirngruber, G.; Prins, R. Dealumination and Realumination of Microcrystalline Zeolite Beta: An XRD, FTIR and Quantitative Multinuclear (MQ) MAS NMR Study. *Phys. Chem. Chem. Phys.* **2004**, *6* (2), 447–452. https://doi.org/10.1039/B311925D.

(49) Wu, P.; Komatsu, T.; Yashima, T. IR and MAS NMR Studies on the Incorporation of Aluminum Atoms into Defect Sites of Dealuminated Mordenites. *J. Phys. Chem.* **1995**, *99* (27), 10923–10931. https://doi.org/10.1021/j100027a036.

(50) Hadjiivanov, K. Chapter Two - Identification and Characterization of Surface Hydroxyl Groups by Infrared Spectroscopy; Jentoft, F. C., Ed.; Advances in Catalysis; Academic Press, 2014; Vol. 57, pp 99–318. https://doi.org/https://doi.org/10.1016/B978-0-12-800127-1.00002-3.

(51) Khalil, I.; Thomas, K.; Jabraoui, H.; Bazin, P.; Maugé, F. Selective Elimination of Phenol from Hydrocarbons by Zeolites and Silica-Based Adsorbents—Impact of the Textural and Acidic Properties. *J. Hazard. Mater.* **2020**, *384*, 121397. https://doi.org/https://doi.org/10.1016/j.jhazmat.2019.121397.

(52) Gallas, J.-P.; Goupil, J.-M.; Vimont, A.; Lavalley, J.-C.; Gil, B.; Gilson, J.-P.; Miserque, O. Quantification of Water and Silanol Species on Various Silicas by Coupling IR Spectroscopy and In-Situ Thermogravimetry. *Langmuir* **2009**, *25* (10), 5825–5834. https://doi.org/10.1021/la802688w.

(53) Sushkevich, V. L.; Ivanova, I. I.; Yakimov, A. V. Revisiting Acidity of SnBEA Catalysts by Combined Application of FTIR Spectroscopy of Different Probe Molecules. *J. Phys. Chem. C* **2017**, *121* (21), 11437–11447. https://doi.org/10.1021/acs.jpcc.7b02206.

(54) Warnken, M.; Lázár, K.; Wark, M. Redox Behaviour of SnO2 Nanoparticles Encapsulated in the Pores of Zeolites towards Reductive Gas Atmospheres Studied by in Situ Diffuse Reflectance UV/Vis and Mössbauer Spectroscopy. *Phys. Chem. Chem. Phys.* **2001**, *3* (10), 1870–1876. https://doi.org/10.1039/B009045J.

(55) Dijkmans, J.; Dusselier, M.; Janssens, W.; Trekels, M.; Vantomme, A.; Breynaert, E.; Kirschhock, C.; Sels, B. F. An Inner-/Outer-Sphere Stabilized Sn Active Site in β-Zeolite:

Spectroscopic Evidence and Kinetic Consequences. *ACS Catal.* **2016**, *6* (1), 31–46. https://doi.org/10.1021/acscatal.5b01822.

(56) Wolf, P.; Valla, M.; Rossini, A. J.; Comas-Vives, A.; Núñez-Zarur, F.; Malaman, B.; Lesage, A.; Emsley, L.; Copéret, C.; Hermans, I. NMR Signatures of the Active Sites in Sn-β Zeolite. *Angew. Chemie Int. Ed.* **2014**, *53* (38), 10179–10183. https://doi.org/10.1002/anie.201403905.

(57) Greenwood, N. N.; Gibbs, T. C. . *Mössbauer Spectroscopy* .; Chapman and Hall: London, 1971.

(58) van der Graaff, W. N. P.; Li, G.; Mezari, B.; Pidko, E. A.; Hensen, E. J. M. Synthesis of Sn-Beta with Exclusive and High Framework Sn Content. *ChemCatChem* **2015**, *7* (7), 1152–1160. https://doi.org/10.1002/cctc.201403050.

(59) Harris, J. W.; Cordon, M. J.; Iorio, J. R. Di; Vega-Vila, J. C.; Ribeiro, F. H.; Gounder, R. Titration and Quantification of Open and Closed Lewis Acid Sites in Sn-Beta Zeolites That Catalyze Glucose Isomerization. *J. Catal.* **2016**, *335*, 141–154. https://doi.org/https://doi.org/10.1016/j.jcat.2015.12.024.

(60) Khalil, I.; Celis-Cornejo, C. M.; Thomas, K.; Bazin, P.; Travert, A.; Pérez-Martínez, D. J.; Baldovino-Medrano, V. G.; Paul, J. F.; Maugé, F. In Situ IR-ATR Study of the Interaction of Nitrogen Heteroaromatic Compounds with HY Zeolites: Experimental and Theoretical Approaches. *ChemCatChem* **2020**, *12* (4), 1095–1108. https://doi.org/https://doi.org/10.1002/cctc.201901560.

(61) Eom, I. Y.; Lee, S.; Hwang, S. Y.; Choi, M. Versatile Post-Synthetic Sn Incorporation into Hierarchically Porous BEA Zeolite for Glucose Isomerization in 1-Butanol. *Microporous Mesoporous Mater.* **2020**, *307*. https://doi.org/https://doi.org/10.1016/j.micromeso.2020.110524.

(62) Boronat, M.; Concepción, P.; Corma, A.; Renz, M.; Valencia, S. Determination of the Catalytically Active Oxidation Lewis Acid Sites in Sn-Beta Zeolites, and Their Optimisation by the Combination of Theoretical and Experimental Studies. *J. Catal.* **2005**, *234* (1), 111–118. https://doi.org/https://doi.org/10.1016/j.jcat.2005.05.023.

(63) Dai, W.; Lei, Q.; Wu, G.; Guan, N.; Hunger, M.; Li, L. Spectroscopic Signature of Lewis Acidic Framework and Extraframework Sn Sites in Beta Zeolites. *ACS Catal.* **2020**, *10* (23), 14135–14146. https://doi.org/10.1021/acscatal.0c02356.

(64) Masai, H.; Ina, T.; Okumura, S.; Mibu, K. Validity of Valence Estimation of Dopants in Glasses Using XANES Analysis. *Sci. Rep.* **2018**, *8* (1), 415. https://doi.org/10.1038/s41598-017-18847-0.

(65) Arii, T.; Kishi, A. The Effect of Humidity on Thermal Process of Zinc Acetate. *Thermochim. Acta* **2003**, *400* (1), 175–185. https://doi.org/https://doi.org/10.1016/S0040-6031(02)00487-2.

(66) Donaldson, J. D.; Moser, W.; Simpson, W. B. 1147. Tin(II) Acetates. *J. Chem. Soc.* **1964**, No. 0, 5942–5947. https://doi.org/10.1039/JR9640005942.

(67) Campo, C. M.; Rodríguez, J. E.; Ramírez, A. E. Thermal Behaviour of Romarchite Phase SnO in Different Atmospheres: A Hypothesis about the Phase Transformation. *Heliyon* **2016**, *2* (5), e00112. https://doi.org/https://doi.org/10.1016/j.heliyon.2016.e00112.

(68) Giefers, H.; Porsch, F.; Wortmann, G. Kinetics of the Disproportionation of SnO. *Solid State Ionics* **2005**, *176* (1), 199–207. https://doi.org/https://doi.org/10.1016/j.ssi.2004.06.006.

(69) Karim, W.; Kleibert, A.; Hartfelder, U.; Balan, A.; Gobrecht, J.; van Bokhoven, J. A.; Ekinci, Y. Size-Dependent Redox Behavior of Iron Observed by in-Situ Single Nanoparticle Spectro-Microscopy on Well-Defined Model Systems. *Sci. Rep.* **2016**, *6* (1), 18818. https://doi.org/10.1038/srep18818.

(70) Navrotsky, A. Nanoscale Effects on Thermodynamics and Phase Equilibria in Oxide Systems. *ChemPhysChem* **2011**, *12* (12), 2207–2215. https://doi.org/10.1002/cphc.201100129.

(71) Jiménez, V. M.; González-Elipe, A. R.; Espinós, J. P.; Justo, A.; Fernández, A. Synthesis of SnO and SnO2 Nanocrystalline Powders by the Gas Phase Condensation Method. *Sensors Actuators B Chem.* **1996**, *31* (1), 29–32.

https://doi.org/https://doi.org/10.1016/0925-4005(96)80012-8.

(72) Zimmermann, E.; Königs, S.; Neuschütz, D. Mass Spectrometric Determination of the Partial Pressures of SnO, Sn2O2 and O2 in Equilibrium with Solid SnO2. *Zeitschrift für Phys. Chemie 209* (2), 271–280. https://doi.org/https://doi.org/10.1524/zpch.1999.209.Part_2.271.

(73) Bigelow, S. L.; Trimble, H. M. The Relation of Vapor Pressure to Particle Size. *J. Phys. Chem.* **1927**, *31* (12), 1798–1816. https://doi.org/10.1021/j150282a003.

(74) Behrndt, K. H. The Enhanced Vapor Pressure of Small Clusters. *Thin Solid Films* **1971**, *7* (6), 415–425. https://doi.org/https://doi.org/10.1016/0040-6090(71)90038-1.

(75) Wang, X.; van Bokhoven, J. A.; Palagin, D. Ostwald Ripening versus Single Atom Trapping: Towards Understanding Platinum Particle Sintering. *Phys. Chem. Chem. Phys.* **2017**, *19* (45), 30513–30519. https://doi.org/10.1039/C7CP05887J.

(76) Castro, R. H. R.; Gouvêa, D. Sintering and Nanostability: The Thermodynamic Perspective. *J. Am. Ceram. Soc.* **2016**, *99* (4), 1105–1121. https://doi.org/https://doi.org/10.1111/jace.14176.

(77) Wang, X.; van Bokhoven, J. A.; Palagin, D. Atomically Dispersed Platinum on Low Index and Stepped Ceria Surfaces: Phase Diagrams and Stability Analysis. *Phys. Chem. Chem. Phys.* **2020**, *22* (1), 28–38. https://doi.org/10.1039/C9CP04973H.

(78) Morgan, K.; Goguet, A.; Hardacre, C. Metal Redispersion Strategies for Recycling of Supported Metal Catalysts: A Perspective. *ACS Catal.* **2015**, *5* (6), 3430–3445. https://doi.org/10.1021/acscatal.5b00535.

(79) Zhang, M.; Wang, M.; Xu, B.; Ma, D. How to Measure the Reaction Performance of Heterogeneous Catalytic Reactions Reliably. *Joule* **2019**, *3* (12), 2876–2883. https://doi.org/https://doi.org/10.1016/j.joule.2019.11.005.

(80) Graaf, G. H.; Scholtens, H.; Stamhuis, E. J.; Beenackers, A. A. C. M. Intra-Particle Diffusion Limitations in Low-Pressure Methanol Synthesis. *Chem. Eng. Sci.* **1990**, *45* (4), 773–783. https://doi.org/https://doi.org/10.1016/0009-2509(90)85001-T.

(81) Zhai, D.; Zhao, L.; Gao, J.; Xu, C. Effect of Temperature on the Diffusion Mechanism of Xylene Isomers in a FAU Zeolite: A Molecular Dynamics Study. *Phys. Chem. Chem. Phys.* **2012**, *14* (20), 7296–7303. https://doi.org/10.1039/C2CP40584A.

(82) Ramanan, H.; Auerbach, S. M.; Tsapatsis, M. Beyond Lattice Models of Activated Transport in Zeolites: High-Temperature Molecular Dynamics of Self-Diffusion and Cooperative Diffusion of Benzene in NaX. *J. Phys. Chem. B* **2004**, *108* (44), 17171–17178. https://doi.org/10.1021/jp0476242.

(83) Bosselet, F.; Sacerdote, M.; Bouix, J.; Mentzen, B. F. The MFI(ZSM-5)/Sorbate Systems. Comparison between Structural, Theoretical and Calorimetric Results. Part I — the MFI/p-Xylene System. *Mater. Res. Bull.* **1990**, *25* (4), 443–450. https://doi.org/https://doi.org/10.1016/0025-5408(90)90179-6.

(84) Karger, J.; Ruthven, D. M. On the Comparison between Macroscopic and n.m.r. Measurements of Intracrystalline Diffusion in Zeolites. *Zeolites* **1989**, *9* (4), 267–281. https://doi.org/https://doi.org/10.1016/0144-2449(89)90071-7.

(85) Wilkenhöner, U.; Gammon, D. W.; van Steen, E. Intrinsic Activity of Titanium Sites in TS-1 and Al-Free Ti-Beta. In *Impact of Zeolites and other Porous Materials on the new Technologies at the Beginning of the New Millennium*; Aiello, R., Giordano, G., Testa, F., Eds.; Studies in Surface Science and Catalysis; Elsevier, 2002; Vol. 142, pp 619–626. https://doi.org/https://doi.org/10.1016/S0167-2991(02)80081-7.

(86) Chiu, J. J.; Pine, D. J.; Bishop, S. T.; Chmelka, B. F. Friedel–Crafts Alkylation Properties of Aluminosilica SBA-15 Meso/Macroporous Monoliths and Mesoporous Powders. *J. Catal.* **2004**, *221* (2), 400–412. https://doi.org/https://doi.org/10.1016/j.jcat.2003.09.005.

(87) Klaewkla, R.; Arend, M.; Hoelderich, W. F. A Review of Mass Transfer Controlling the Reaction Rate in Heterogeneous Catalytic Systems. In *Mass Transfer*; Nakajima, H., Ed.; IntechOpen: Rijeka, 2011. https://doi.org/10.5772/22962.

(88) Conrad, S.; Wolf, P.; Müller, P.; Orsted, H.; Hermans, I. Influence of Hydrophilicity on the Snβ-Catalyzed Baeyer–Villiger Oxidation of Cyclohexanone with Aqueous Hydrogen Peroxide. *ChemCatChem* **2017**, *9* (1), 175–182. https://doi.org/10.1002/cctc.201600893.

(89) Yilmaz, B.; Müller, U.; Feyen, M.; Maurer, S.; Zhang, H.; Meng, X.; Xiao, F.-S.; Bao, X.; Zhang, W.; Imai, H.; Yokoi, T.; Tatsumi, T.; Gies, H.; De Baerdemaeker, T.; De Vos, D. A New Catalyst Platform: Zeolite Beta from Template-Free Synthesis. *Catal. Sci. Technol.* **2013**, *3* (10), 2580–2586. https://doi.org/10.1039/C3CY00073G.

(90) De Baerdemaeker, T.; Yilmaz, B.; Müller, U.; Feyen, M.; Xiao, F.-S.; Zhang, W.; Tatsumi, T.; Gies, H.; Bao, X.; De Vos, D. Catalytic Applications of OSDA-Free Beta Zeolite. *J. Catal.* **2013**, *308*, 73–81. https://doi.org/https://doi.org/10.1016/j.jcat.2013.05.025.

(91) Taufiqurrahmi, N.; Mohamed, A. R.; Bhatia, S. Nanocrystalline Zeolite Beta and Zeolite Y as Catalysts in Used Palm Oil Cracking for the Production of Biofuel. *J. Nanoparticle Res.* **2011**, *13* (8), 3177–3189. https://doi.org/10.1007/s11051-010-0216-8.

(92) Eyring, H. The Activated Complex in Chemical Reactions. *J. Chem. Phys.* **1935**, *3* (2), 107–115. https://doi.org/10.1063/1.1749604.

(93) Turcas, R.; Lakk-Bogáth, D.; Speier, G.; Kaizer, J. Kinetics and Enantioselectivity of the Baeyer-Villiger Oxidation of Cyclohexanones by Chiral Tetrapyridyl Oxoiron(IV) Complex. *Inorg. Chem. Commun.* **2018**, *92*, 141–144. https://doi.org/https://doi.org/10.1016/j.inoche.2018.04.024.

(94) Bates, J. S.; Bukowski, B. C.; Harris, J. W.; Greeley, J.; Gounder, R. Distinct Catalytic Reactivity of Sn Substituted in Framework Locations and at Defect Grain Boundaries in Sn-Zeolites. *ACS Catal.* **2019**, *9* (7), 6146–6168. https://doi.org/10.1021/acscatal.9b01123.

(95) Crépeau, G.; Montouillout, V.; Vimont, A.; Mariey, L.; Cseri, T.; Maugé, F. Nature, Structure and Strength of the Acidic Sites of Amorphous Silica Alumina: An IR and NMR Study. *J. Phys. Chem. B* **2006**, *110* (31), 15172–15185. https://doi.org/10.1021/jp062252d.

(96) Onfroy, T.; Clet, G.; Houalla, M. Quantitative IR Characterization of the Acidity of Various Oxide Catalysts. *Microporous Mesoporous Mater.* **2005**, *82* (1), 99–104. https://doi.org/https://doi.org/10.1016/j.micromeso.2005.02.020.

(97) Douvalis, A. P.; Polymeros, A.; Bakas, T. IMSG09: A57Fe-119Sn Mössbauer Spectra Computer Fitting Program with Novel Interactive User Interface. *J. Phys. Conf. Ser.* **2010**,

217, 12014. https://doi.org/10.1088/1742-6596/217/1/012014.

For Table of Contents Only